Biological methane oxidation is catalyzed by a mononuclear copper center in particulate methane monooxygenase

Authors: Matthew O. Ross[1], Fraser MacMillan[2], Jingzhou Wang[4], Alex Nisthal[4], Thomas J. Lawton[1], Barry D. Olafson[3], Stephen L. Mayo[4], Amy C. Rosenzweig[1]*, Brian M. Hoffman[1]*

Affiliations:

[1]Departments of Molecular Biosciences and of Chemistry, Northwestern University, Evanston, IL 60208, USA

[2]Henry Wellcome Unit for Biological Electron Paramagnetic Resonance Spectroscopy, School of Chemistry, University of East Anglia, Norwich NR4 7TJ, United Kingdom

[3]Protabit LLC, 1010 E. Union St., Ste. 110, Pasadena, CA 91106, USA

[4]Divisions of Biology, and Chemistry and Chemical Engineering, California Institute of Technology, MC 114-96, 1200 East California Boulevard, Pasadena, CA 91125, USA

*Corresponding author. Email: amyr@northwestern.edu (A.C.R.); bmh@northwestern.edu (B.M.H.)

Abstract: Bacteria that oxidize methane to methanol are central to mitigating emissions of methane, a highly potent greenhouse gas. The nature of the copper active site in their primary metabolic enzyme, particulate methane monooxygenase (pMMO), has been controversial, owing to seemingly contradictory biochemical, spectroscopic, and crystallographic results. Biochemical and advanced electron paramagnetic resonance spectroscopic characterization now resolves the location and nuclearity of the pMMO copper cofactors: there are two monocopper sites, one in the soluble PmoB subunit at the previously assigned active site (Cu_B) and one ~2 nm away in the membrane-bound PmoC subunit (Cu_C). Based on these results, we propose that a monocopper site is able to catalyze methane oxidation under the ambient pressure and temperature conditions at which these bacteria grow.

One Sentence Summary: Nature's predominant aerobic methane-oxidizing enzyme employs a monocopper active site.

Main Text:

Methane is both a potent greenhouse gas and a readily-available energy source (*1-3*). Methanotrophic bacteria use enzymes called methane monooxygenases (MMOs) to activate dioxygen and break a 105 kcal/mol C-H bond in methane to produce methanol at ambient pressure and temperature (*1*). By contrast, current industrial catalysis processes for this reaction require tremendous pressure and temperature (>1000 K). Understanding how enzymes catalyze this reaction is critical to developing catalysts that function at moderate temperature and pressure (*4-8*).

The most common MMO is the membrane-bound, copper-dependent particulate enzyme (pMMO) (*9*). Multiple pMMO crystal structures reveal a trimeric assembly of protomers, each comprising two predominantly transmembrane subunits (PmoA and PmoC) and one

transmembrane subunit with a large periplasmic domain (PmoB) (Fig. 1A) (*10-13*). Three copper-binding sites have been detected in the pMMO structures. *(i)* A monocopper ligated by His48 and His72 (bis-His site, Fig. S1) is observed only in the *Methylococcus capsulatus* (Bath) pMMO structure. *(ii)* All structures contain copper coordinated by the amino terminal histidine of PmoB (His33), as well as His137 and His139 (Cu_B site, *M. capsulatus* (Bath) numbering, Fig. 1A). On the basis of extended X-ray absorption fine structure (EXAFS) data, this site was initially modeled as dicopper in some (*10, 11*), but not all (*11-13*), structures. *(iii)* A bound copper ion is found in the PmoC subunit coordinated by residues Asp156, His160, and His173 (*14*).

The nuclearity, ligation, and location of the pMMO copper active site remain controversial. This controversy mostly stems from theories that catalytically relevant metallocofactors are lost through the pMMO isolation and purification procedure, consistent with the substantially lower activity of pMMO after isolating the membranes from the organism ($\lesssim$17% of that in vivo) (*9, 13*), the variable metal content observed across different crystal structures and biochemical handling procedures, and the fact that enzymatic activity has not been demonstrated *in crystallo*, calling into question the physiological and catalytic relevance of observed metallocofactors. Catalysis has been proposed to occur at a tricopper site in PmoA (*15*) (not observed crystallographically), a diiron center at the PmoC metal-binding site (*16*), and the Cu_B site (*17*). We now report that pMMO contains two conserved monocopper sites and define their coordination environments, showing that a monocopper site catalyzes methane oxidation.

To circumvent any complications arising from loss of copper cofactors through enzyme purification, we probed the pMMO Cu(II) sites in the enzyme's natural environment (in vivo) in whole cells of *M. capsulatus* (Bath) grown on ^{15}N and ^{63}Cu by electron paramagnetic resonance (EPR) spectroscopy. Under copper-replete conditions, pMMO is highly expressed (~20% of total protein (*16*)). Therefore, any Cu(II) sites within the protein should be present in such high quantity as to dominate the in vivo EPR spectrum. Indeed, prior EPR spectra of whole cell methanotroph samples exhibited a type 2 Cu(II) EPR signal that was attributed to pMMO-bound Cu(II) based on the high Cu(II) concentration and similarity to the EPR spectrum of isolated methanotroph membranes (*18-20*). We too observe this type 2 Cu(II) EPR signal in the whole cell (Vivo-pMMO) EPR spectrum of ^{15}N, ^{63}Cu enriched *M. capsulatus* (Bath) (Fig. 1) (**g** = [2.242, 2.068, 2.035]; ^{63}Cu hyperfine splitting A_1 = 570 MHz or 190 x 10^{-4} cm^{-1}). The presence of four ^{15}N equatorial ligands is indicated by a five-line ^{15}N hyperfine splitting of the low-field g_1 Cu(II) hyperfine transition (Fig. S2). The ratio of $g_1/A_1(cm^{-1})$ = 118 cm indicates a highly planar equatorial Cu coordination (*21-23*).

We characterized the nitrogenous ligands of this Cu(II) species with electron nuclear double resonance (ENDOR) spectroscopy. ^{15}N Davies ENDOR spectra collected near g_1 exhibited strongly-coupled ^{15}N resonances corresponding to two similar directly-coordinated Cu(II) ligands (Fig. 2A) ($|A_1(^{15}N)| \sim 48, 53$ MHz); Gaussian fitting and quantitation of the resonances indicated that the ν_+ peak with the larger coupling is three times more intense than the other ν_+ peak (Fig. 2B, Tables S1, S2). The near-equivalence of these couplings combined with the quantitation is evidence for a Cu(II) site with four (determined by the 3:1 intensity ratio) equatorial ^{15}N ligands bound in a square plane (*24*). ^{15}N Mims (Doan/ReMims) ENDOR spectra collected near g_1 also exhibit weakly-coupled ^{15}N resonances from the remote (non-coordinated) ^{15}N of histidyl imidazoles bound to Cu(II) (Fig. 2A) (*25*) ($|A_1(^{15}N)| \sim 1.7, 2.3$ MHz) in a 1:2 intensity ratio (Fig. 2B, Tables S1, S2). Thus, of the four N ligands defined by the ^{15}N Davies ENDOR, three are histidyl imidazole side chains. Consistent with this assignment, ^{1}H Davies ENDOR measurements showed non-exchangeable signals with couplings of $A_2 \sim 4.5$ and 2.5 MHz, characteristic of the ring protons of Cu(II)-bound histidyl imidazole (Fig. S3, Table S1)

(*26*). Additional broad, exchangeable ^{1}H signals with couplings $|A_1| \sim |A_2| \sim 10$ MHz are as expected for protons of -NH_2 coordinated to Cu(II) (Fig. S3, Table S1) (*26*).

To assign the location of this Cu(II) species, we examined the histidine residues in all pMMO crystal structures, looking for sites where three imidazoles and an -NH_2 could simultaneously coordinate a Cu(II). The only location that can supply this spectroscopically-defined ligand set is the Cu_B site (Fig. 1, Fig. S4) which provides three imidazole nitrogens from His33, His137, and His139 as well as the -NH_2 of His33. The correspondence between this ligand assemblage and the EPR/ENDOR-defined ligation definitively resolves the longstanding controversy of whether Cu_B contains a mono- or dinuclear center: Cu_B is a monocopper site.

To characterize any pMMO copper sites that might be maintained in vivo in the reduced, Cu(I) state, we allowed them to air oxidize by solubilizing and purifying *M. capsulatus* (Bath) pMMO via size exclusion chromatography (Purified-pMMO). The Cu_B(II) signal persisted in Purified-pMMO, but another Cu(II) signal appeared, denoted Cu_C (Fig. 2, $\boldsymbol{g}$ = [2.30, 2.07, 2.05]; ^{63}Cu hyperfine splitting A_1 = 440 MHz or 147 x 10^{-4} cm^{-1}), as previously observed in purified pMMO EPR samples (*13, 27*). The larger Cu_C(II) g_1/A_1 = 156 cm is characteristic of a distorted (flattened) tetrahedral geometry (*28, 29*). In support of the conclusion that pMMO houses only monocopper centers, we have also found that an optical spectrum previously proposed to result from a dicopper center (*30*) is instead associated with a product of O_2 or H_2O_2 oxidation of ascorbate in the presence of methanol and copper (Fig. S5), and additional support for this conclusion is discussed in the SI.

Reduction of Purified-pMMO (Reduced/Purified pMMO) effectively eliminated the Cu_C(II) EPR signal, leaving a Cu_B(II) signal virtually identical to that observed in vivo (Fig. 2), similar to previous reports of the reduction of pMMO localized in methanotroph membranes (*20, 31*), and with unchanged ^{15}N ENDOR responses (Fig. 2), confirming that the Cu_B(II) site is unchanged during purification. The nonexchangeable signals from the imidazole ring protons and the exchangeable signals from protons attributed to -NH_2 (Fig. S3B) are also unchanged. We further addressed the four-N ligation of Cu_B by EPR/ENDOR characterization of Reduced/Purified-pMMO incubated with $H_2{}^{17}O$. The characteristic ^{17}O ENDOR response of an equatorially coordinated H_xO is absent, showing that Cu_B does not have such a ligand (Fig. S6). The experiments did exhibit the ^{17}O signal characteristic of an axial $H_x{}^{17}O$ on Cu_B, however, meaning the geometry of Cu_B(II) is best described as square pyramidal.

To determine the location of the Cu_C(II) site, we measured Cu(II)-Cu(II) distances in Purified-pMMO via double electron-electron resonance (DEER) spectroscopy. The background-corrected DEER dipolar evolution for Purified-pMMO and corresponding Cu(II)-Cu(II) distance distribution obtained by Fourier transformation (*32*) are shown in Fig. 3. There are two peaks in the distance distribution, a major peak at a distance of 4.5 nm and a minor peak at 2.8 nm. The 2.8 nm peak is very weak and, as shown in Fig. S7, is extremely variable in intensity depending on the procedure used to analyze the time-wave, whereas the 4.5 nm distance is robust, and indeed its counterpart can be clearly seen as the sinusoidal modulation of the time evolution trace. Thus, we consider the shorter distance peak to be an artifact of the data processing.

We compared the 4.5 nm distance to the Cu-Cu distances in the *M. capsulatus* (Bath) pMMO crystal structure, which contains two metal binding sites besides the Cu_B site: the bis-His site in PmoB (Fig. S1) and the PmoC metal binding site (Fig. 1). If the Cu_C(II) EPR signal corresponded to the bis-His site, a second robust Cu-Cu distance of ~3.2 nm (Cu_C to Cu_C) would be expected as well as the ~4.4 nm distance (interprotomer Cu_B to Cu_C), contrary to observation. However, assignment of Cu_C(II) to the PmoC site predicts a single Cu-Cu distance of ~4.4 nm (Cu_C to Cu_C, Fig. 3C) in agreement with the data; an intraprotomer ~2 nm Cu_B to Cu_C distance must be too short to be observed. Overall, the distance measurements indicate that Cu_C is not

located in the bis-His site and instead is located in the PmoC metal binding site. This assignment is supported by ^{15}N ENDOR measurements on Purified-pMMO (Fig. 3), which are consistent with the PmoC Cu_C ligand assemblage depicted in Fig. 1. ^{1}H and ^{17}O ENDOR further indicate that Cu_C contains a H_xO ligand (Figs. S3, S6) as modeled in two pMMO crystal structures (*11, 12*).

The characterization of these two monocopper sites in pMMO reopens the question of the identity of the catalytic site. The mononuclear Cu_B site exhibits saturated equatorial coordination, with strongly-bound N-ligands, and thus is unlikely to undergo O_2-binding/activation without alteration. However, addition of nitrite (a known inhibitor of methane oxidation (*33*)) perturbs the Cu_C(II) signal (Fig. S8). This observation, combined with the fact that the Verrucomicrobial pMMOs possess none of the Cu_B-ligating amino acids (*34*), prompted us to reinvestigate the activity of the spmoB protein. This recombinantly expressed construct comprises the soluble portion of the *M. capsulatus* (Bath) PmoB subunit and is a model for native PmoB copper binding. It was reported to exhibit methane oxidation activities 1-10% that of pMMO (*17, 27*), the only direct evidence identifying Cu_B as the active site.

To probe Cu_B reactivity in a more stable protein platform, we generated several constructs of spmoB (Fig. S9) that did not require refolding after expression (unlike spmoB, which expresses into inclusion bodies (*17*)), at least one of which assembled a Cu_B site very similar to Cu_B(II) by EPR (Fig. S10A), unlike spmoB, which exhibits a different EPR spectrum (*27*), and tested the new constructs and the original spmoB for activity (Figs. S10B, S11). These proteins indeed produced ^{13}C-methanol when assayed for ^{13}C-methane oxidation. However, the amount of ^{13}C-methanol produced was not significantly affected by mutating the Cu_B site, by altering the temperature, reaction time, protein concentration, or by using an enzyme incapable of oxidizing methane (Fig. S11C-E). The reactivity may instead be attributed to the ability of duroquinol to reduce O_2 and generate H_2O_2. H_2O_2 in turn produces $OH^{\bullet}$ via autolysis and via Fenton and Haber-Weiss chemistry (*35-38*), which then oxidizes methane. These findings eliminate the support for a Cu_B active site.

Instead there is evidence that Cu_C, located in the site illustrated in Fig. 1, may be the site of O_2-binding and methane oxidation. Such a model would be consistent with the suggested presence of a displaceable equatorial solvent ligand on Cu_C, as needed for O_2-binding/activation, and the absence of the Cu_B site in the Verrucomicrobial pMMOs. Finally, mutation of any Cu_C ligand in a pMMO homolog from *Mycobacterium* NBB4 (hydrocarbon monooxygenase) resulted in complete loss of activity (*39*). Cu_C is thus inferred to be the active site of hydrocarbon substrate binding and oxidation, but Cu_B nonetheless is important. Replacement of a Cu_B ligand diminished overall activity significantly (by 80%), but the variant's affinity for alkane substrate was within error of wild type for two of the three alkanes assayed (*39*), indicating Cu_B does play a functional role, but is not the site of hydrocarbon substrate binding and oxidation.

References and Notes:

1. M. O. Ross, A. C. Rosenzweig. *J. Biol. Inorg. Chem.* **22**, 307-319 (2017).
2. A. R. Brandt *et al. Science* **343**, 733-735 (2014).
3. *Inventory of U.S. greenhouse gas emissions and sinks: 1990–2015* (2017).
4. Q. Fei *et al. Biotechnol. Adv.* **32**, 596-614 (2014).
5. R. Horn, R. Schlögl. *Catal. Lett.* **145**, 23-39 (2015).
6. B. E. R. Snyder, M. L. Bols, R. A. Schoonheydt, B. F. Sels, E. I. Solomon. *Chem. Rev.* **118**, 2718-2768 (2018).
7. M. S. Khan, J. H. Park, Y. D. Chaniago, M. Lee. *Energy Procedia* **61**, 599-602 (2014).

8. J. Gao *et al. Science* **348**, 686-690 (2015).
9. T. J. Lawton, A. C. Rosenzweig. *J. Am. Chem. Soc.* **138**, 9327-9340 (2016).
10. R. L. Lieberman, A. C. Rosenzweig. *Nature* **434**, 177-182 (2005).
11. S. M. Smith *et al. Biochemistry* **50**, 10231-10240 (2011).
12. S. Sirajuddin *et al. J. Biol. Chem.* **289**, 21782-21794 (2014).
13. S. Y. Ro *et al. J. Biol. Chem.* **293**, 10457-10465 (2018).
14. Zinc has also been observed in this site, although only when the zinc was added exogenously.
15. V. C. C. Wang *et al. Chem. Rev.* **117**, 8574-8621 (2017).
16. M. Martinho *et al. J. Am. Chem. Soc.* **129**, 15783-15785 (2007).
17. R. Balasubramanian *et al. Nature* **465**, 115-119 (2010).
18. S. S. Lemos, M. L. P. Collins, S. S. Eaton, G. R. Eaton, W. E. Antholine. *Biophys. J.* **79**, 1085-1094 (2000).
19. H. Yuan, M. L. P. Collins, W. E. Antholine. *J. Am. Chem. Soc.* **119**, 5073-5074 (1997).
20. H. H. Nguyen *et al. J. Biol. Chem.* **269**, 14995-15005 (1994).
21. U. Sakaguchi, A. W. Addison. *J. Chem. Soc.*, 600-608 (1979).
22. R. Pogni, M. C. Baratto, A. Diaz, R. Basosi. *J. Inorg. Biochem.* **79**, 333-337 (2000).
23. R. N. Patel *et al. Inorganica Chim. Acta* **362**, 4891-4898 (2009).
24. M. Iwaizumi, T. Kudo, S. Kita. *Inorg. Chem.* **25**, 1546-1550 (1986).
25. M. M. Dicus *et al. J. Am. Chem. Soc.* **132**, 2037 (2010).
26. P. Manikandan, B. Epel, D. Goldfarb. *Inorg. Chem.* **40**, 781-787 (2001).
27. M. A. Culpepper, G. E. Cutsail III, W. A. Gunderson, B. M. Hoffman, A. C. Rosenzweig. *J. Am. Chem. Soc.* **136**, 11767-11775 (2014).
28. H. Yokoi. *Bull. Chem. Soc. Jpn.* **47**, 3037-3040 (1974).
29. T. P. Cheeseman, D. Hall, T. N. Waters. *J. Chem. Soc. A*, 685-693 (1966).
30. M. A. Culpepper, G. E. Cutsail III, B. M. Hoffman, A. C. Rosenzweig. *J. Am. Chem. Soc.* **134**, 7640-7643 (2012).
31. H. Yuan, M. Lynne Perille Collins, W. E. Antholine. *J. Inorg. Biochem.* **72**, 179-185 (1998).
32. G. Jeschke *et al. Appl. Magn. Reson.* **30**, 473-498 (2006).
33. G. Nyerges, L. Y. Stein. *FEMS Microbiol. Lett.* **297**, 131-136 (2009).
34. H. J. Op den Camp *et al. Environmental Microbiology Reports* **1**, 293-306 (2009).
35. C. C. White, R. K. Chain, R. Malkin. *Biochim. Biophys. Acta* **502**, 127-137 (1978).
36. C. E. Taylor. *Prepr. Pap.-Am. Chem. Soc., Div. Fuel Chem.* **48**, 876 (2003).
37. E. Cadenas, A. Boveris, C. I. Ragan, A. O. M. Stoppani. *Arch. Biochem. Biophys.* **180**, 248-257 (1977).
38. H. Ikai *et al. Antimicrob. Agents Chemother.* **54**, 5086-5091 (2010).
39. E. F. Liew, D. Tong, N. V. Coleman, A. J. Holmes. *Microbiology* **160**, 1267-1277 (2014).

Acknowledgments: We thank Dr. George E. Cutsail III, Prof. Megen A. Culpepper, and Prof. Heather W. Pinkett for helpful discussions, as well as the expert analysis of the Gaussian fitting and above and beyond effort provided by an anonymous reviewer.
Funding: Supported by NIH grants GM118035 (A. C. R.), GM111097 (B. M. H.), 5T32GM008382 (M. O. R.), and NSF grant 1534743 (S. L. M., B. O.; A. C. R.). F. M. was supported by a Royal Society Wolfson Research Merit Award.

Author contributions: M.O.R, F.M., A.N., T.J.L., S.L.M., A.C.R. and B.M.H. designed experiments. M.O.R., F.M., J.W., and A.N. carried out experiments. M.O.R, A.C.R., and B.M.H. wrote the manuscript.

Competing interests: The authors declare no competing financial interests.

Data and materials availability: All data are available in the manuscript or the supplementary material.

Supplementary Materials:

Materials and Methods

Tables S1-S3

Figs. S1-S16

References 40 - 62

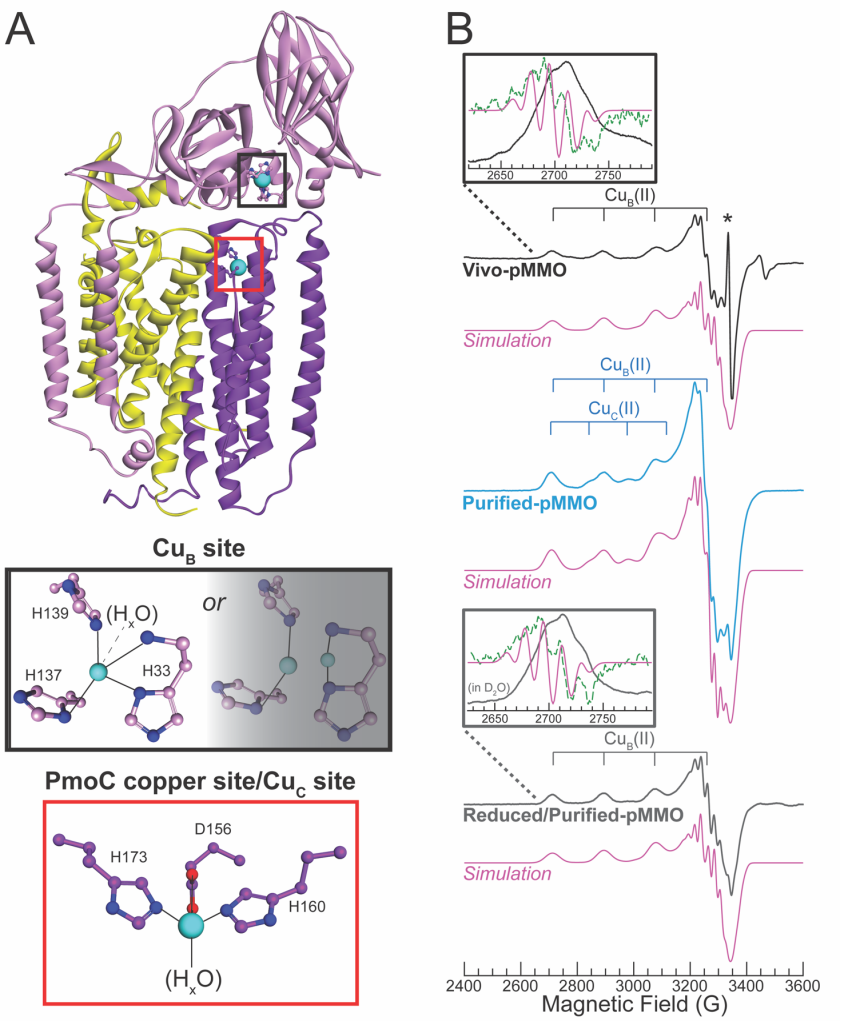

Fig. 1. Structure of one pMMO protomer as well as X-band continuous wave (CW) EPR of Vivo- (showing Cu_B(II)), Purified- (showing Cu_B(II) and Cu_C(II)), and Reduced/Purified-pMMO (showing Cu_B(II)). (**A**) Single protomer from the *M. capsulatus* (Bath) pMMO crystal structure (DOI: 10.2210/pdb3rgb/pdb) (*11*), showing PmoA (yellow), PmoB (pink), PmoC (purple), Cu (cyan), N (blue), and O (red) atoms. ***Inset, top***: The Cu_B site modeled as monocopper and dicopper. ***Inset, bottom***: The PmoC metal site (which we have now determined to be the Cu_C site) occupied with copper. (**B**) EPR spectra with simulations of the Cu_B(II) (Vivo- and Reduced/Purified-pMMO) and Cu_B(II) plus 0.32 equivalents Cu_C(II) (Purified-pMMO) shown below each spectrum. ***Insets*** depict lowest-field Cu hyperfine transition with computed second derivative (green dotted line) and second derivative of the simulation (pink solid line). Asterisk denotes an organic radical species in Vivo-pMMO. This radical is not present in Purified- or Reduced/Purified-pMMO. In the Reduced/Purified-pMMO (***inset***), the two lowest field ^{15}N hyperfine lines are unresolved, likely due to a small amount of Cu_C(II). Spectra and simulation parameters are listed in Table S1, and collection conditions are provided in the SI. Rapid-passage Q-band absorption-display CW EPR spectra shown in Fig. S12. Unless otherwise noted, the concentrations of all EPR/ENDOR samples of Purified- or Reduced/Purified-pMMO were 300-500 μM. All pMMO spectra were measured on ^{63}Cu, ^{15}N-labeled pMMO samples.

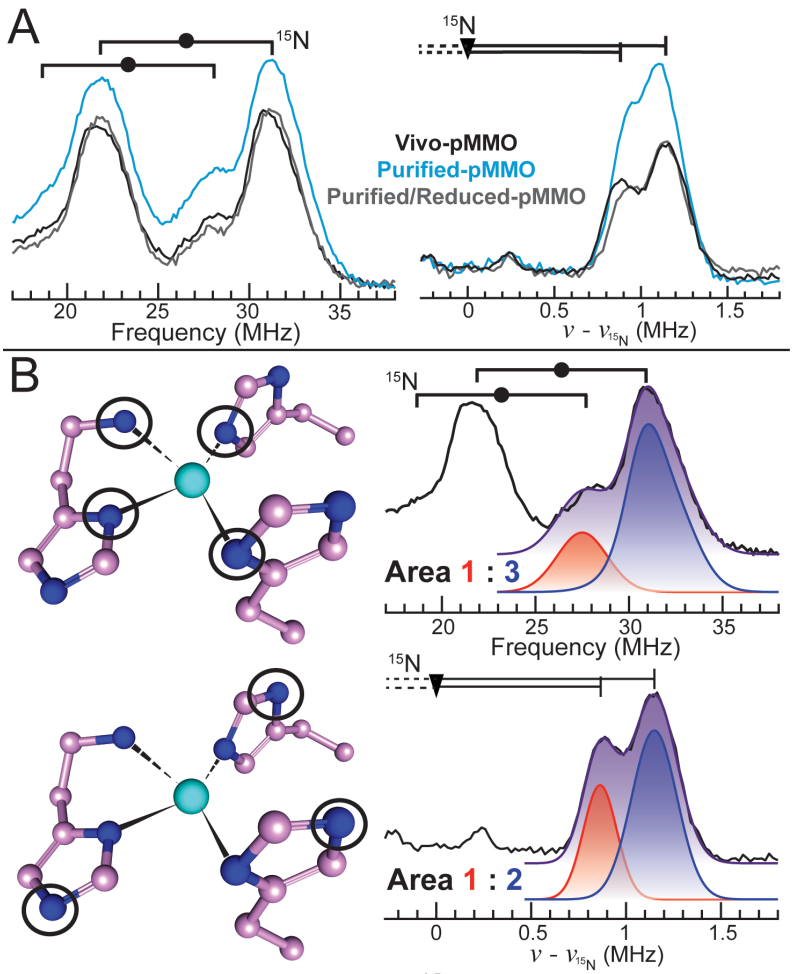

Fig. 2. Characterization of Cu_B(II) and Cu_C(II) ^{15}N ligation by ENDOR. (**A**) Q-band pulsed ENDOR measurements collected at g_1 for (***left***) strongly- and (***right***) weakly-coupled ^{15}N nuclei, using Davies and Doan/ReMims ENDOR, respectively. ***Left*****:** Goalpost widths indicate twice the ^{15}N Larmor frequency ($\nu_{^{15}N}$), and the filled circles define half the hyperfine coupling magnitude ($|A/2|$). ***Right:*** The triangle defines $\nu_{^{15}N}$ and the distance from triangle to vertical line equals $|A/2|$. (**B**) ***Left***: Circled nitrogen atoms produce the observed ENDOR responses to the right of each Cu_B site. ***Right***: Overlay of Vivo-pMMO experimental spectra with individual (red and blue) and summed (purple) Gaussian functions used to quantitate ^{15}N resonance peaks. Parameters are listed in Tables S1 and S2, and collection conditions are provided in the SI. While only the ν_+ peak is shown for the Vivo-pMMO weakly-coupled ^{15}N ENDOR response, both ν_- and ν_+ are shown in Fig. S13.

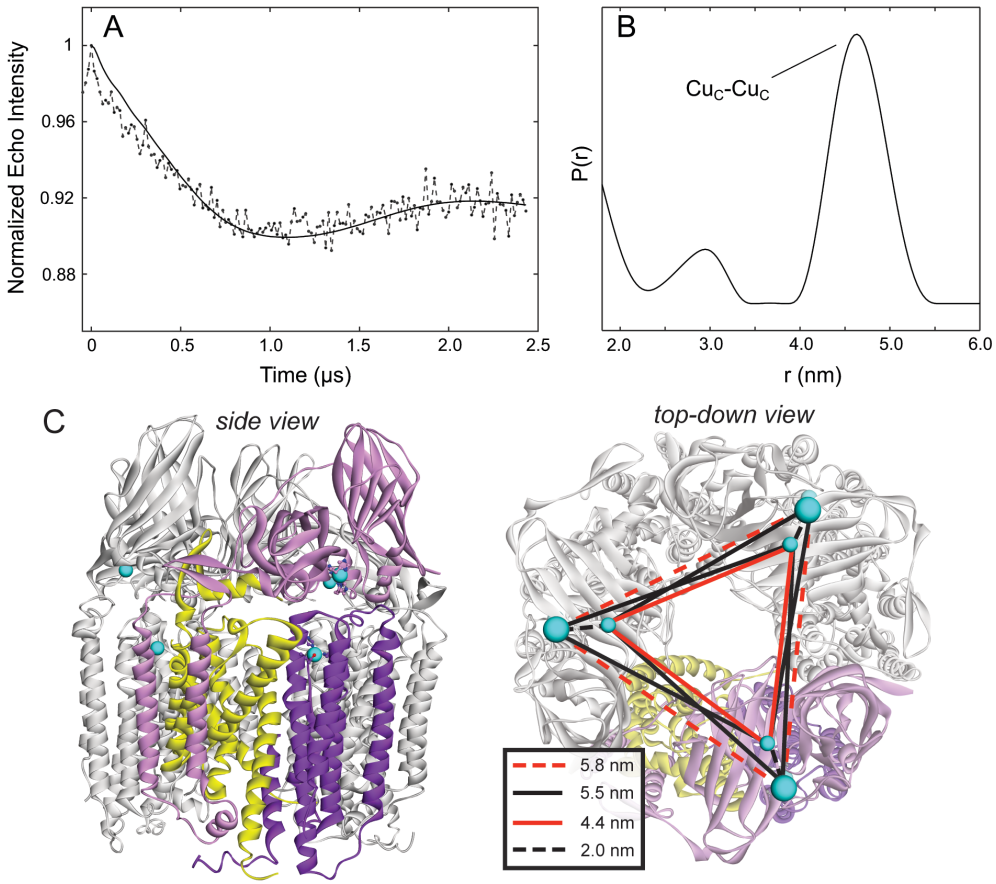

Fig. 3. Purified-pMMO Cu(II)-Cu(II) four pulse DEER distance measurements with (**A**) normalized first-order homogeneous background decay-corrected dipolar evolution (solid line is a fitting of the dipolar evolution using DeerAnalysis2016) and (**B**) Cu(II)-Cu(II) distance distributions calculated using DeerAnalysis 2016. The measured Cu(II)-Cu(II) distance (4.5 nm) is consistent with the distances expected for Cu$_C$(II) in the PmoC variable metal site and excludes the presence of Cu(II) in the bis-His site; if Cu$_C$(II) was located in the bis-His site, a 3.2 nm Cu(II)-Cu(II) distance would be predicted (Fig. S1). (**C**) Crystal structure of the *M. capsulatus* (Bath) pMMO trimer with same coloring as Fig. 1 (except two protomers are globally colored gray), and the various predicted Cu-Cu distances (***inset***).

Supplementary Materials for

Biological methane oxidation is catalyzed by a mononuclear copper center in particulate methane monooxygenase

Matthew O. Ross[1], Fraser MacMillan[2], Jingzhou Wang[3], Alex Nisthal[3], Stephen L. Mayo[3], Amy C. Rosenzweig[1]*, Brian M. Hoffman[1]*

*Corresponding author. Email: amyr@northwestern.edu (A.C.R.); bmh@northwestern.edu (B.M.H.)

This PDF file includes:

Materials and Methods

Production of $^{63}CuSO_4$

50 mg aliquots of ^{63}CuO (Cambridge Isotope Laboratories) were dissolved in 1.5 mL of 3 M trace metal grade H_2SO_4 while heating at 60-80°C and shaking at 300 rpm. The reaction was judged to be complete when no black CuO particles were visible in the blue $CuSO_4$ solution (after several days).

Growth of *M. capsulatus* (Bath) and preparation of Vivo-pMMO EPR sample

Isotopically enriched ^{15}N, ^{63}Cu-*M. capsulatus* (Bath) was grown in a 12 L bioreactor as described previously with minor modifications (*13, 40*). Briefly, cells were grown in a solution of 3.9 mM phosphate buffer, pH 6.8, 40 µM NaFe(III)EDTA, trace element solution, 50 µM $^{63}CuSO_4$ and 1X ^{15}N-nitrate mineral salts (NMS) (Cambridge Isotopes Laboratories, potassium ^{15}N-nitrate) with a constant flow of 1:4 methane-to-air gas mix. NaOH and H_2SO_4 were used to maintain the growth medium pH between 6.7 and 7.4. Cells were harvested by centrifugation (6,000 x g for 20 min at 4°C) at OD_{600} of 11.3. Of this yield, 0.75 g of cell pellet was set aside on ice, while the rest was frozen in liquid nitrogen and stored at -80°C. To prepare whole cell EPR samples, the 0.75 g of cell pellet was resuspended in 50 mL of 12.2 mM dibasic sodium phosphate, 7.8 mM monobasic sodium phosphate, 5 mM magnesium chloride, pH 7.0 and centrifuged at 4°C, 10,000 x g, for 10 min, as done previously (*41*). The supernatant was poured off, the wash and centrifugation procedure was repeated, and the supernatant was again poured off. The cells were resuspended in 200 µL of phosphate buffer, and this suspension was then aliquoted into a Wilmad quartz X-band EPR tube (Sigma Aldrich) and custom quartz Q-band EPR tube (~180 µL and ~80 µL, respectively, as with all EPR samples in this study). EPR samples were frozen in liquid nitrogen, where they were stored until analysis. Natural abundance *M. capsulatus* (Bath) was grown and harvested under similar conditions except natural abundance $CuSO_4$ and NMS were used for the growth medium instead of $^{63}CuSO_4$ and ^{15}N-NMS.

pMMO purification and X-band Continuous Wave (CW) and Q-band EPR/ENDOR sample preparation

M. capsulatus (Bath) cells were resuspended in 25 mM PIPES, 250 mM NaCl, pH 7.2-7.3 and lysed by sonication (either using 90% power setting, 1 s on, 1 s off sonication for 10 min, or a 90% power setting, 1 s on, 2 s off sonication for 8 min) and membranes containing pMMO were isolated, solubilized, and purified by size exclusion chromatography (using a 120 mL Superdex 200 equilibrated in 25 mM PIPES, 250 mM NaCl, 0.02 % DDM, pH 7.2-7.3, 1 mL/min flow rate) as described previously (*13, 42*), although for this study the solubilized membranes were concentrated to 2 mL (rather than 1 mL) before running size exclusion chromatography and the PIPES buffer used throughout (i.e. with and without DDM) was kept at pH 7.2-7.3 (rather than pH 7.0). After size exclusion chromatography, the sample was concentrated via centrifugation at 5,000 x g, at 4°C using an Amicon spin concentrator; samples were subsequently either frozen in liquid nitrogen and stored at -80°C until use, or, to make Purified-pMMO EPR samples, aliquoted into X- or Q-band EPR tubes and frozen in liquid nitrogen. To generate Reduced/Purified-pMMO, Purified-pMMO was degassed and made anaerobic on a Schlenk line, and then brought into a Coy anaerobic glovebox. 10-12 protein equivalents of sodium ascorbate in anaerobic 25 mM PIPES, pH 7.5 or 25 mM PIPES, 250 mM NaCl, 0.02 % DDM, pH 7.5 were added to the protein solution. Reduced/Purified-pMMO samples were allowed to equilibrate for at least 1 hr at room temperature in the glovebox before

being aliquoted into X- or Q-band EPR tubes which were frozen in liquid nitrogen in the glovebox. While the Cu_C(II) EPR signal was always significantly more diminished by ascorbate reduction than the Cu_B(II) signal, occasionally some Cu_C(II) was apparent even after this procedure. When this occurred, the sample was thawed anaerobically, and ascorbate was added until the Cu_C(II) signal was no longer evident. For Purified-pMMO in D_2O samples, the protein was buffer exchanged into 25 mM PIPES, 250 mM NaCl, 0.02% DDM buffer in D_2O (99.9%-D, Sigma-Aldrich), pD 7.3. To prepare Reduced/Purified-pMMO in D_2O, Purified-pMMO in D_2O was anaerobically reduced as above except the ascorbate was prepared in the deuterated buffer mentioned above (made anaerobic). Unless otherwise noted, the concentrations of all EPR/ENDOR samples of Purified- or Reduced/Purified-pMMO were comparable, only varying between 300 and 500 µM.

For Purified-pMMO incubated with nitrite, $NaNO_2$ was dissolved in 25 mM PIPES, 250 mM NaCl, 0.02% DDM, pH 7.2 to generate a 4 M $NaNO_2$ stock solution. 100 µL of this stock was then added to 100 µL of natural abundance Purified-pMMO, and the sample was incubated at room temperature for 2 hr and 15 min. The sample was then transferred to an X-band EPR tube and flash frozen in liquid nitrogen.

For Purified- and Reduced/Purified-pMMO samples incubated with $H_2{}^{17}O$, the enzyme was desalted into 2X wash buffer (50 mM PIPES, 500 mM NaCl, 0.04% DDM, pH 7.2) using a PD-10 desalting column at 4°C. The protein was concentrated to 90 µL, ~630 µM protein using a 100 kDa cutoff Amicon filter. The protein was then diluted with 90 µL of 90% ^{17}O-enriched H_2O (Sigma Aldrich). To generate the Purified-pMMO in $H_2{}^{17}O$, 80 µL of this sample was put in a Q-band EPR tube inside of a cryotube, parafilmed to make airtight, and then left in the dark at room temperature overnight. To generate the Reduced/Purified-pMMO, with the remaining 100 µL of pMMO, the protein was made anaerobic using a Schlenk line and brought into the glovebox, where it was treated with 12 protein equivalents of ascorbate (in anaerobic 25 mM PIPES, 250 mM NaCl, 0.02% DDM, pH 7.2). The protein was incubated overnight in the dark at room temperature in the glovebox. In the morning this sample was transferred to a Q-band EPR tube. Both Q-band samples were flash frozen in liquid nitrogen in the morning (the anaerobic sample was flash frozen in the glovebox).

Design, expression, and purification of spmoB constructs and NeMCO

spmoB was recombinantly expressed in *E. coli* into inclusion bodies and refolded in 20 mM Tris, 250 mM NaCl, pH 8.0 as described previously (*17*), except Tris base was used instead of Tris-Cl.

To optimize spmoB solubility and create a solubly expressing spmoB construct, we redesigned the artificial flexible linker that connects PmoB subdomain 1 (PmoB D1) and subdomain 2 (PmoB D2) in spmoB, and tested various combinations of N- and C-terminal soluble tag attachments to spmoB. To reduce flexibility and aggregation propensity, the original linker in spmoB was replaced with the following sequence: pmoB(residues 169-182)-GEPS-Protein GB1-GE-pmoA(residues 170-203)-S-pmoB(residues 267-281) (Fig. S9), in which Protein GB1 is the B1 domain of Protein G. Solubility improvements were screened by the split-GFP assay and confirmed by SDS-PAGE (*43*). Out of the screened variants, constructs Con7 with a Set12 tag (Set12 is is the T7B9 peptide (*44*))at both C- and N-termini, and SUMO7 (Con7 with an additional N-terminal SUMO tag) were identified to be solubly expressed at ≥10 mg/L in *E. coli* (Fig. S9). In order to test whether the foldedness of the copper-binding PmoB D1 affects the activity, error-prone PCR was performed on the PmoB D1 subdomain alone, and the resulting variants were selected by a twin-arginine translocation (TAT) pathway-based ampicillin survival assay, which has been shown to isolate variants with improved folding (*45, 46*). From

this assay, a single amino acid mutation variant (PmoB D1_E75D) was identified to grant host expression *E. coli* cells with improved ampicillin survival rate than PmoB D1_WT, and assembled back to the SUMO7 construct to create SUMO7_E75D. To validate that methanol produced in the methane oxidation activity assays was a result of enzymatic turnover at the previously reported pMMO active site (Cu_B), we produced two negative control constructs which should have exhibited no methane oxidation activity. For SUMO7_3A, the three Cu_B residues (H33, H137, and H139) were mutated to alanine to abrogate copper binding at this site. The second negative control was a multicopper oxidase (NeMCO, derived from *Nitrosomonas europaea*)(*47*) that does not oxidize methane.

SUMO7, SUMO7_E75D, SUMO7_3A, and NeMCO were expressed in chemically-competent *E. coli* BL-21(DE3)Gold cells by either auto induction or IPTG induction. For auto induction, 5 mL of overnight culture in LB with 100 µg/mL of ampicillin (Amp100) was inoculated into1 L of ZYM-5052 media with Amp100 at 37℃ until OD_{600} hit 0.5, and then at 20℃ for 24 hours to express protein (*48*). For IPTG induction, 1 L of LB/Amp100 was inoculated by 5 mL of overnight culture at 37℃, and induced by 1 mM IPTG at OD_{600} between 0.6 and 1.0. Expression was then conducted at 27℃ for 4 hours. Post-expression culture was transferred to a capped bottle, supplemented with water to replace the headspace gas, and treated with 1x ZYM-5052 sugar solution together with 1 mM of $CuSO_4$ for 2 hours to allow *in-vivo* copper loading (*48*). Cells were then harvested, lysed by a cell disruptor, and centrifuged at 15,000 x g for 40 min. Soluble protein was then purified by Strep-Tactin beads (IBA) and stored in either 1x PBS (137 mM NaCl, 2.7 mM KCl, 10 mM Na_2HPO_4, 1.8 mM KH_2PO_4, pH 7.4) or 1x TBS (50 mM Tris, 150 mM NaCl, pH 7.6). Protein was concentrated by 30kDa MWCO spin-filters (Amicon) to ≤ 1 mL volume before further analysis.

For the refolded SUMO7 sample, soluble protein was expressed in C41(DE3) chemically competent *E. coli* cells in ZYM-5052 autoinduction media with 50-100 µg/mL ampicillin at 37°C (*48*). After the OD_{600} reached ~0.5, the temperature was lowered to 18°C for overnight expression. Cells were harvested by centrifugation, frozen in liquid nitrogen and stored at -80°C until use. Cells were then thawed and resuspended in 50 mM Tris, 150 mM NaCl, pH 8.0 and lysed by sonication; cell debris was pelleted by centrifugation, and the protein was purified via Strep-Tactin column (IBA-GMBH). After purification, the protein was unfolded in 8 M urea at a protein concentration of 0.7 mg/mL (protein concentration determined using the Pierce™ 660 nm assay (VWR International) and a molecular weight of 69.292 kDa) and was subsequently refolded in the presence of $CuSO_4$ following a previously described protocol (*27*). After refolding, the protein was ultracentrifuged for 40 min at 125,000 x g, 4°C, and concentrated using a 10 kDa cutoff Amicon spin concentrator. Aliquots of 50 µM SUMO7 were then immediately tested for methane oxidation activity, and the rest of the protein was frozen in liquid nitrogen and stored at -80°C until later use. To prepare the refolded SUMO7 X-band EPR sample, protein was thawed, concentrated using an Amicon spin concentrator to 250 µM, transferred to a Wilmad quartz X-band EPR tube and frozen in liquid nitrogen.

Optical spectroscopy

All optical spectroscopy measurements were performed on an Agilent 8453 spectrophotometer with an Agilent 89090A Peltier temperature controller.

Methane oxidation activity assays

All Purified- and Reduced/Purified-pMMO preparations used to produce paramagnetic resonance spectroscopy samples were verified as active (capable of catalyzing methane

oxidation) using a very slightly adjusted bicelle-reconstitution ^{13}C methane oxidation activity assay (*13*). Duroquinol was generated from duroquinone (VWR International) as described previously (*49*). For all methane oxidation activity assays, 100 µL of 2.6-8.0 mg/mL purified pMMO in 3-6% DMPC:CHAPSO 2.8:1 bicelle solution (Molecular Dimensions or Anatrace), or 100 µL of spmoB/spmoB construct (concentrations and length of reaction provided in figures), were mixed with a small scoop of duroquinol placed into sealed septa top vials (Agilent). A 2:1 ratio of ^{13}C-methane (Sigma-Aldrich) and air, totaling 3 mL, was injected into the top. Reactions were incubated in a water bath shaking at 200 rpm (10 min at 30°C for pMMO, otherwise temperature and time of reaction are provided in figures) after which point the reaction were either immediately stopped using 500 µL of chloroform spiked with 1 mM dichloromethane or were frozen and later thawed; upon thawing 500 µL of chloroform spiked with 1 mM dichloromethane was added to the vial. The amount of $^{12/13}C$-methanol after reaction was determined using a PoraBOND Q column (Agilent) on an Agilent 7890B/5977A MSD GC/MS instrument monitoring the 33 m/z ion (^{13}C-methanol) and 31 m/z ion (^{12}C-methanol) relative to the 49 m/z ion (dichloromethane internal standard) as described previously (*13*). The GC oven temperature holding times were varied to adjust for changing retention times over the life of the GC column. Absolute ^{13}C methanol concentrations were determined by comparison of ^{13}C-methanol peak intensities to those of known concentration ^{13}C-methanol (Sigma-Aldrich) standards in buffer. A signal-to-noise cutoff of 1.0 for the ^{13}C-methanol integrated peak area was used to distinguish real signal from noise; samples with signal-to-noise less than 1.0 were treated as 0 µM ^{13}C-methanol.

X-band CW-EPR and Q-band ENDOR measurements

All CW X-band EPR measurements (except those of SUMO7) were performed using a Bruker ESP-300 spectrometer with a liquid helium flow Oxford Instruments ESR-900 cryostat. SUMO7 EPR was measured on a modified Varian E-4 with a liquid nitrogen finger-dewar at 77 K. All wide scans spanning ≥1000 G were background subtracted. Collection conditions (Fig. 1, wide and inset scans): 9.36-9.37 GHz microwave frequency, 90 s per scan, 320 ms time constant, 12.5 G modulation amplitude, temperature at 20 K, at least 5 scans. SI spectra collection conditions are provided below the figures. All EPR simulations were performed using EasySpin (*50*).

Pulsed ENDOR measurements were collected at ~2 K in a liquid helium immersion dewar on a spectrometer described elsewhere, with SpinCore PulseBlaster ESR_PRO 400MHz digital word generator, and Agilent Technologies Acquiris DP235 500 MS/sec digitizer using SpecMan software (*51, 52*). For all ^{1}H and strongly-coupled ^{15}N ENDOR measurements, a Davies [π–T_{RF}–$\pi/2$–τ–π–τ–echo] pulse sequence was employed, in which T_{RF} denotes the interval during which the RF was applied. For weakly-coupled remote ^{15}N ENDOR measurements, a Doan/ReMims [$\pi/2$–τ_1–$\pi/2$–T_{RF}–$\pi/2$–τ_2–π–(τ_1 + τ_2)–echo] or a Mims [$\pi/2$–τ–$\pi/2$–T_{RF}–$\pi/2$–τ–echo] pulse sequence was employed (*53*). Hyperfine coupling (A) of I = 1/2 nuclear spin (^{15}N and ^{1}H) and S = 1/2 electron spin (Cu(II)) produce an ENDOR spectrum given by the equation $\nu_{\pm} = |\nu_n \pm \frac{A}{2}|$, where ν_+ and ν_- are the high and low frequency peaks of the doublet, respectively, while ν_n is the Larmor frequency for the nucleus (n). For Fig. 2, collection conditions were as follows: (strongly-coupled ^{15}N) 34.592 GHz microwave frequency, 100 ms repetition time, π = 80 ns, τ = 600 ns, T_{RF} = 15 µs, and RF tail = 5 µs; (weakly-coupled ^{15}N) 34.608 GHz microwave frequency, 20 ms repetition time, π = 60 ns, τ_1 = 200 ns, τ_2 = 400 ns, T_{RF} = 60 µs, and RF tail = 10 µs, ^{15}N-Larmor corrected. The sign of the ^{15}N hyperfine coupling was determined through the Pulsed ENDOR Saturation Recovery (PESTRE) experiment (Fig. S14), which provides the absolute sign of A/g_n (*54*).

X-band pulsed DEER sample preparation and measurements

75 µL of 360 µM natural abundance Purified-pMMO in 2X wash buffer (50 mM PIPES, 500 mM NaCl, 0.04% DDM, pH 7.2) was aliquoted into a Wilmad quartz X-band EPR tube. The altered buffer conditions do not affect the Cu(II) ligation (Fig. S15). X-band pulsed EPR spectra were recorded on a Bruker E680 spectrometer (Bruker, Rheinstetten, Germany) using a Bruker MD5-W1 EPR probehead equipped with a self-modified cryogen-free cryostat (Advanced Research Systems Inc, Macungie, PA, USA). The microwave pulses were amplified using a 1kW-TWT (Applied Systems Engineering Inc., Fort Worth, TX, USA). All EPR experiments were carried out at 17K. The field-swept spectrum was obtained by integrating the Hahn echo signal as a function of the magnetic field after a two-pulse sequence.

For the 4-pulse PELDOR experiments recorded at 17 K, pulse lengths were 20 nsec for $\pi/2$ and 20 nsec for π. The pump pulse length was 16 nsec and $\Delta\nu$ ($\nu_{obs} - \nu_{pump}$) was 80 MHz, with the detection field set at a *g* value of 2.07. The pulse separation τ_1 was 200 nsec while τ_2 varied between 2500-3500 ns, and the echo signals were integrated using a video amplifier bandwidth of 20 MHz. The pump pulse was stepped out by 16 nsec for a total number of points in T that depended upon the τ_2 used. Nuclear modulation artifacts were suppressed using a systematic variation of the interpulse delay time τ_1 and an appropriate phase cycling routine.

Supplemental Text

Discrepancy between the paramagnetic resonance analysis and previous EXAFS data

Previous EXAFS scattering was fit with a short Cu-Cu distance (~2.5-2.6 Å) indicative of a dicopper center. However, all three possible oxidation states of a dicopper center, Cu(II)-Cu(II), Cu(II)-Cu(I), or Cu(I)-Cu(I), are not consistent with the current analysis. Two Cu(II) ions at ~2.5-2.6 Å separation, with no magnetic interaction between them, would produce a large dipolar splitting in the EPR spectrum that is not observed. A (anti)ferromagnetically coupled Cu(II)-Cu(II) center would not contribute to the paramagnetic resonance spectroscopy, but we do not observe the characteristic charge transfer optical absorbance features associated with the superexchange coupling pathway requisite to forming such centers (*55, 56*). To the best of our knowledge, there is no dicopper Cu(I)-Cu(I) metal site in biology that does not oxidize in air, so if a Cu(I)-Cu(I) site were present, it would oxidize to either Cu(II)-Cu(I) or Cu(II)-Cu(II) during the aerobic purification procedure. In addition, in previous studies from our laboratory (*13, 57*), Cu^{2+} EPR spin quantitation of purified pMMO indicated that nearly all Cu in the protein is EPR active Cu^{2+}, inconsistent with a dicopper Cu(I)-Cu(I) site. Finally, we consider a Cu(II)-Cu(I) center. As noted previously, we do not observe any of the characteristic features associated with such valence-delocalized center (*27*). As described in the main text, the 4 N ligands in the Cu_B site all are bound to the single Cu(II) giving rise to the Cu_B EPR signal; the terminal NH_2 and the side chains of His33, His137, and His139 are coordinated in a square plane of equatorial coordination. Thus, there are no ligands available to coordinate a second copper ion, excluding the possible presence of a valence-localized Cu(II)-Cu(I) site. Viewed from a different perspective, the Cu(II) EPR signal from spmoB differs from that of Cu_B in pMMO, yet the EXAFS for both proteins was fit with the same Cu-Cu scattering interaction (within ~0.1 Å) (*17*). It is implausible that the two samples with distinct copper centers coincidentally both contain dicopper centers with the same Cu-Cu distance.

Table S1. Summary of the paramagnetic spectroscopic parameters of the Cu_B and Cu_C sites.*

	g_1, g_2, g_3	Cu A_1, A_2, A_3 (MHz)	Directly Coord. ^{15}N A_1, A_2§ (MHz)†	Remote ^{15}N $\lvert A_1 \rvert$ (MHz)		^1H A_1, A_2 (MHz)‡
Cu_B	2.242, 2.068, 2.035	570, 30, 14	-48, -54 -53, -54 -53, -54 -53, -66	1.7 2.3 2.3 N/A	His33-NH_2 $H_{\varepsilon-1}$ $H_{\varepsilon-2}$ H_β H_δ	~10, ~10 - , 4.5 - , 2.5 - , ~1 - , ~1
Cu_C	2.30, 2.07, 2.05	440, 40, 20	-48, -54 -53, -66	~2	H_xO	~8, ~10

***** For simulations featuring the full Vivo-, Purified, and Reduced/Purified-pMMO EPR spectra in Fig. 1 using the above parameters, anisotropic *g*-strain (for both Cu_B and Cu_C, EasySpin *g*-strain parameters 0, 0, 0.03 for g_3, g_2, g_1, respectively) was employed, with additional isotropic 14 G and 25 G fwhm Gaussian line width broadening for Cu_B and Cu_C, respectively. For simulations depicted in insets, the Cu_B g_1 value was changed very slightly to 2.252, and isotropic 13 G fwhm Gaussian line width broadening was employed, with no anisotropic broadening. Simulation of Purified-pMMO represents the sum of 1 Cu_B equivalent and 0.32 Cu_C equivalents. For comparison to ^{14}N ENDOR measurements, see Table S3.

§ Strongly-coupled ^{15}N A_2 ENDOR measurements are shown in Fig. S16. The four features seen in these spectra are plausibly, but not uniquely assigned as listed.

† PESTRE experiments determined that all directly-coordinated ^{15}N possess positive spin density $\rho > 0$ (Fig. S14); the ^{15}N hyperfine couplings are therefore negative because the ^{15}N nuclear $g_n < 0$.

‡ The ^1H ENDOR assignment to individual C-H/N-H bonds of the histidine imidazole ring and amine are made by analogy to Cu(II)(histidine)$_2$ complex (*26*).

Table S2. Vivo-pMMO ^{15}N A_1 Gaussian fitting parameters used in Fig. 2.*

	Resonance	Gaussian Function Parameters			R^2
Remote ^{15}N	Red	$k = 30.32$ $a_1 = 0.08824$ $b_1 = 0.8631$			0.997
	Blue§	$a_2 = 0.1194$ $b_2 = 1.149$			
Directly-coord. ^{15}N	Red	$k = 6.57$ $a_1 = 1.341$ $b_1 = 27.5$			0.9938
	Blue†	$a_2 = 1.329$ $b_2 = 32.28$	$a_3 = 1.75$ $b_3 = 31.13$	$a_4 = 0.9132$ $b_4 = 30.77$	

* The colors red or blue define the color of the Gaussian curves shown in Fig. 2, which were used to fit the ^{15}N ν_+ resonance. R^2 values correspond to the fit of the full normalized Gaussian function to the experimental spectrum over a range of $\nu - \nu_{^{15}N}$= 0.627-1.604 MHz for remote ^{15}N, and over a range of 25.651-28.043 MHz for directly-coordinated ^{15}N resonance. The MatLab Curve Fitting tool was used fit the Gaussian function parameters, using the following equations: normalized Gaussian function,

remote ^{15}N: $$f(x) = k\left[\frac{1}{a_1\sqrt{2\pi}}e^{-\frac{(x-b_1)^2}{2(a_1)^2}} + 2\frac{1}{a_2\sqrt{2\pi}}e^{-\frac{(x-b_2)^2}{2(a_2)^2}}\right],$$

directly-coordinated ^{15}N:

$$f(x) = k\left(\frac{1}{a_1\sqrt{2\pi}}e^{-\frac{(x-b_1)^2}{2(a_1)^2}} + \frac{1}{a_2\sqrt{2\pi}}e^{-\frac{(x-b_2)^2}{2(a_2)^2}} + \frac{1}{a_3\sqrt{2\pi}}e^{-\frac{(x-b_3)^2}{2(a_3)^2}} + \frac{1}{a_4\sqrt{2\pi}}e^{-\frac{(x-b_4)^2}{2(a_4)^2}}\right),$$

where k is a factor that scales calculated and experimental spectra, a_n is related to the width of the peak (in MHz), and b_n defines the center of the Gaussian peak (in MHz).

§ In Fig. 2 the blue peak intensity is twice that produced by simply using the parameters to account for the fact that the function used for total fitting also doubles the intensity of this peak relative to the red peak

† Blue, directly-coordinated ^{15}N resonance function is defined by the sum of three equal area Gaussian functions

Table S3. Conversion of ^{15}N hyperfine coupling to equivalent ^{14}N hyperfine coupling for comparison with past characterization of Purified pMMO.

	^{15}N $\lvert A_1 \rvert$ (MHz)		^{14}N $\lvert A_1 \rvert$ (MHz)	Source
^{15}N-labelled	A_1-$^{15}N_1$	48	[*34*]†	This study
	A_1-$^{15}N_2$	53	[38]†	
Natural abundance	N/A		35.5	(*27*)

† Values in brackets correspond to hyperfine coupling predicted based on conversion between the two nuclear gyromagnetic ratios: $A_{^{15}N} = 1.403(A_{^{14}N})$, (*58*). The two distinguishable ^{15}N hyperfine couplings observed with ^{15}N-labelled Purified-pMMO are not resolved from one another in the natural abundance Purified-pMMO ^{14}N ENDOR spectrum from (*27*), presumably due to the substantial quadrupolar broadening of the ^{14}N ENDOR response.

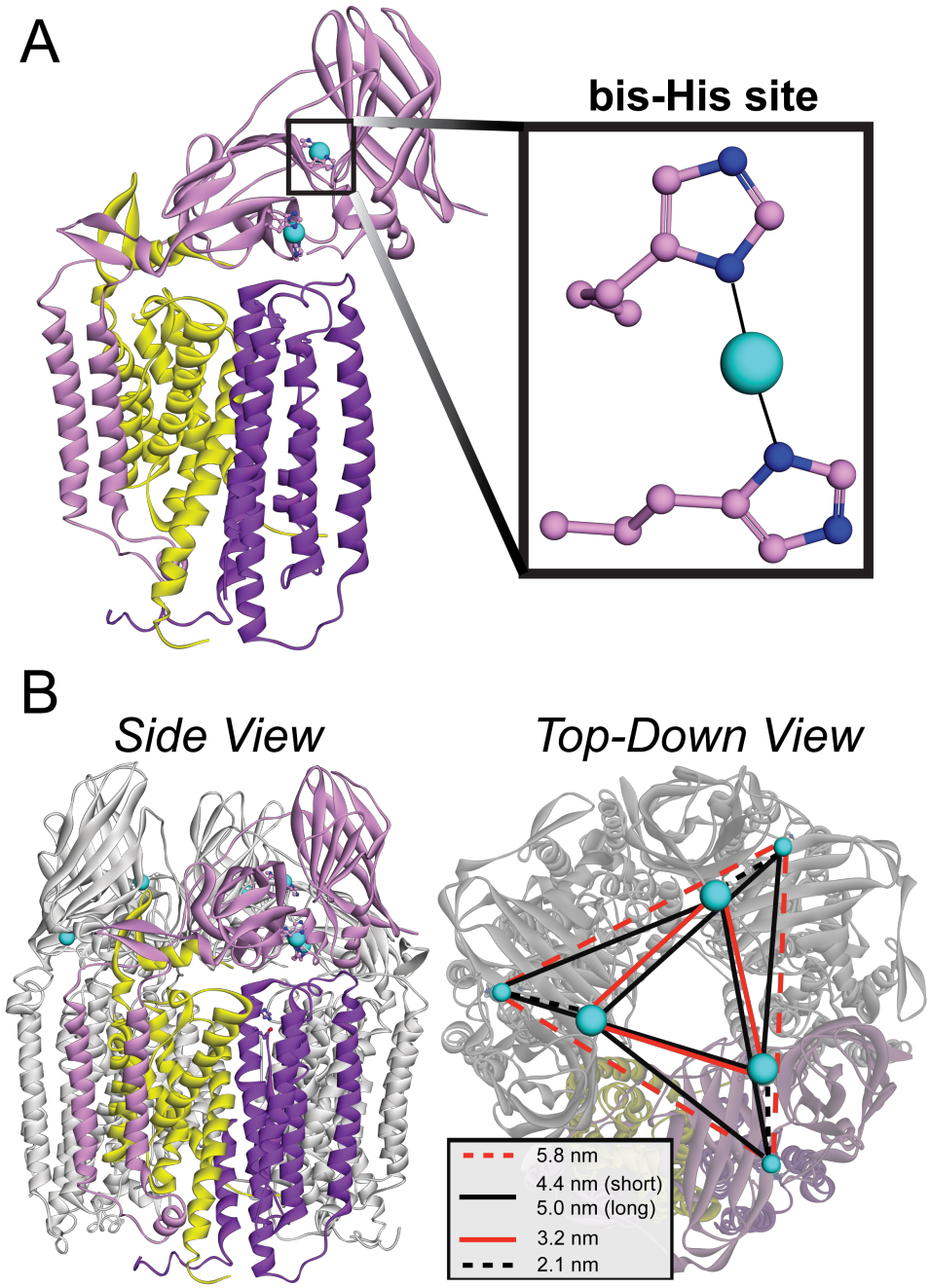

Fig. S1. (**A**) One protomer of the *M. capsulatus* (Bath) pMMO modeled with an unoccupied PmoC metal site and a Cu-bound bis-His site. ***Inset***: A closer view of the bis-His site. (**B**) Full pMMO trimer with Cu_B to bis-His Cu distances (***inset***).

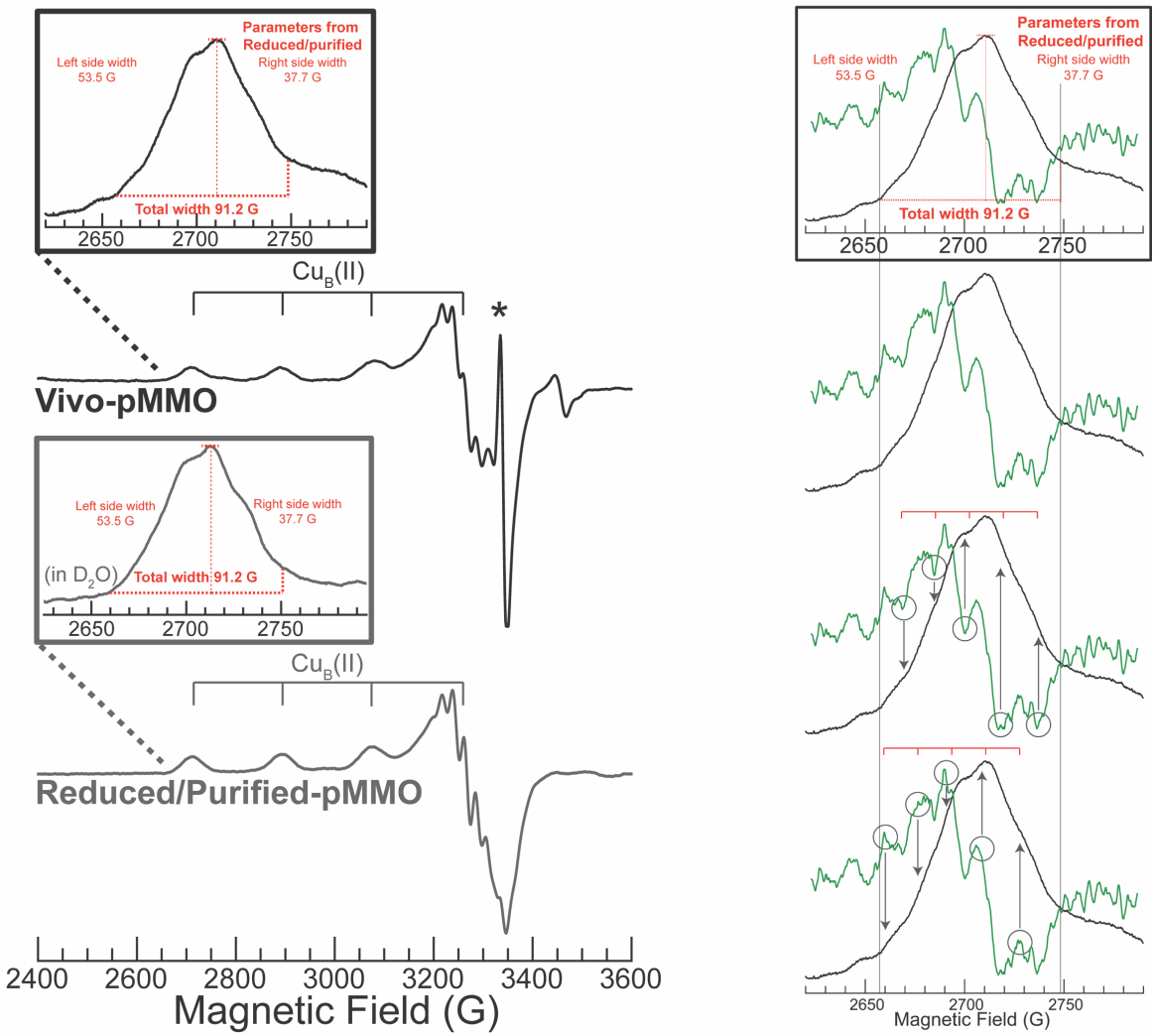

Fig. S2. Support for the assignment of 4 directly coordinated N equatorial ligands on Cu_B from the EPR shown in Fig. 1. We first distinguished the region corresponding to Cu_B(II) resonance from resonance attributable to the contaminant paramagnet(s) clearly present at the high and low field edge of the Vivo-pMMO single Cu(II) hyperfine line in this region. Toward this end, we measured the total width of the low field Cu_B(II) hyperfine line in Reduced/Purified-pMMO (left, bottom), since this spectrum does not contain these contaminants. Specifically, we measured the width of the total resonance to the left and to the right of the hyperfine transition maximum height peak. We then used these bounds to define the Cu_B(II) resonance in Vivo-pMMO (left, top and right). There are 5 evenly spaced local minima in the second derivative (green) of the experimental spectrum, as well as the 5 corresponding evenly spaced local maxima, as shown by the circles in the figure below, indicative of 5 hyperfine lines. Additionally, these peak and valley features clearly correspond to the expected splittings on the absorption-like experimental spectrum. 5 hyperfine lines can only be accounted for by 4 approximately equivalent $I = 1/2$ nuclei, such as that expected from 4 ^{15}N equatorial ligands.

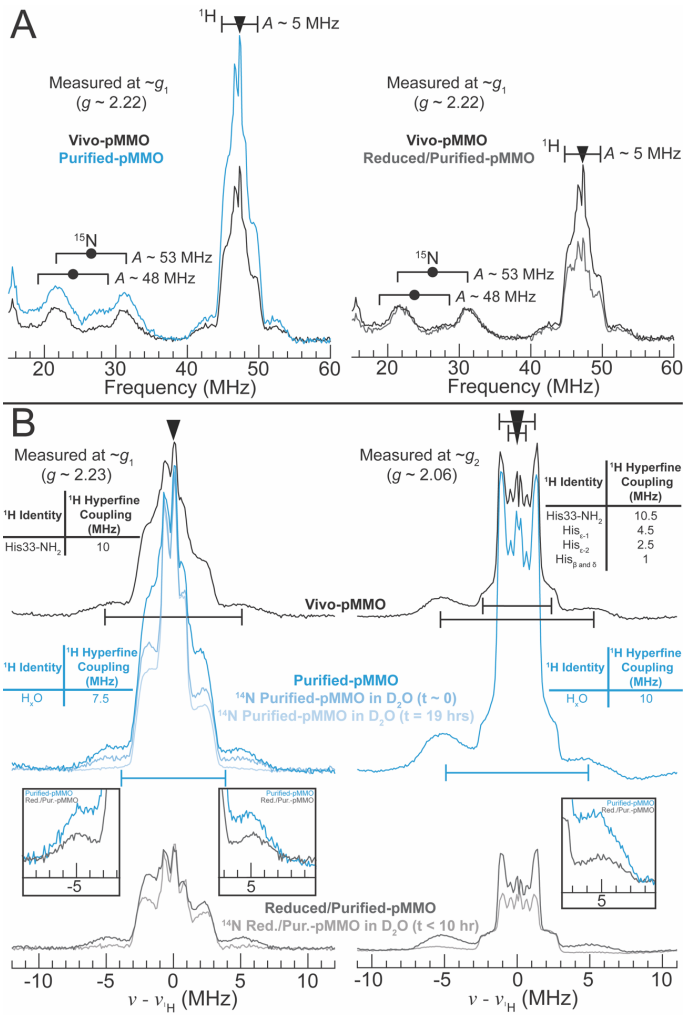

Fig. S3. ^{1}H and ^{15}N Davies ENDOR for Vivo-, Purified-, and Reduced/Purified-pMMO. Times incubated in D_2O buffer are listed. (**A**) ENDOR measurements simultaneously probing ^{15}N and ^{1}H, with heights normalized to echo intensity. Filled circle defines half the ^{15}N hyperfine coupling magnitude ($|A/2|$) and associated goalpost width indicates twice the ^{15}N Larmor frequency ($\nu_{^{15}N}$); triangle defines the ^{1}H Larmor frequency ($\nu_{^1H}$) and associated goalpost width defines hyperfine coupling magnitude ($|A|$). The weakly-coupled ^{1}H resonance (A < ~5 MHz) in Vivo-pMMO that is less intense in Reduced/Purified-pMMO is attributed to solvent H_xO near the Cu_B site in vivo that is not present in purified enzyme. Collection conditions: 34.5-34.6 GHz microwave frequency, 100 ms repetition time, π = 200 ns, τ = 600 ns, T_{RF} = 60 μs, and RF tail = 10 μs. (**B**) ^{1}H Larmor-centered ^{1}H ENDOR measured at (***left***) g_1 and (***right***) g_2, where triangle defines the ^{1}H Larmor frequency ($\nu_{^1H}$) and goalpost width defines the hyperfine coupling magnitude ($|A|$). Vivo-, Purified-, and Reduced/Purified-pMMO ENDOR intensities were normalized to ENDOR intensities in (**A**). ***Insets*** highlight the increased intensity and altered lineshape of the Purified-pMMO large coupling ^{1}H resonance relative to Reduced/Purified-pMMO, evidence for a coordinated H_xO (with hyperfine coupling, $|A_1|$ ~ 8 MHz, $|A_2|$ ~ 10 MHz) (*59*) on Cu_C. Collection conditions: 34.5-34.8 GHz microwave frequency, 100 ms repetition time, π = 200 ns, τ = 600 ns, T_{RF} = 60 μs, and RF tail = 10 μs.

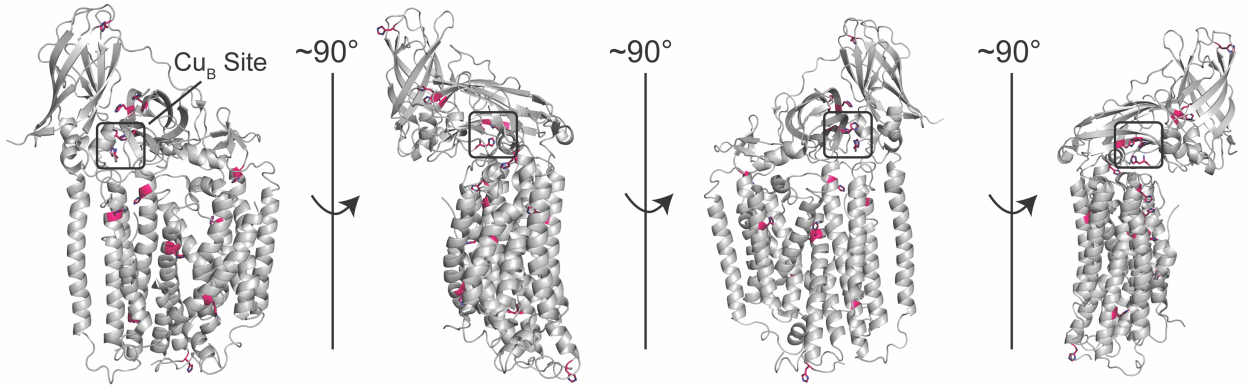

Fig. S4. One protomer of *M. capsulatus* (Bath) pMMO from the crystal structure in Fig. 1, with all protomers colored gray, shown from several angles, with His residues highlighted in pink. The Cu_B site is the only site where three His side chains come together.

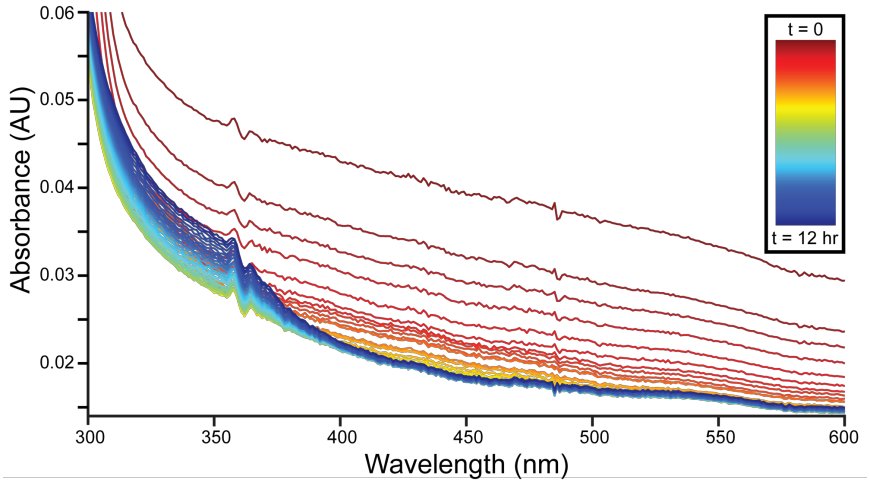

Fig. S5. UV-Vis spectra monitoring formation of the 345 nm optical feature. A sample of 25 mM PIPES, 250 mM NaCl, 0.02% DDM, pH 7.2 (*M. capsulatus* (Bath) Purified-pMMO wash buffer) with 120 μM $CuSO_4$ (to represent the Cu equivalents present in the pMMO sample used previously (*30*)) and 4 μM methanol (to represent background-level contamination present to varying degrees in most pMMO preparations) was made anaerobic in a sealed cuvette and incubated with 5 Cu(II) equivalents of ascorbate for 30 min. 2.5 Cu(II) equivalents of H_2O_2 were then added using a gas-tight syringe, and optical spectra were measured every 15 min for 12 hr at room temperature. Formation of the 345 nm feature is observed on the timescale defined previously (*30*) and can be attributed to ketal derivatives of dehydroascorbic acid generated by the reaction of ascorbate and H_2O_2 (*60*). The drifting baseline in early timepoints is an instrument artifact. The variable intensity of the 345 nm feature previously observed upon mutation of the Cu_B ligands is likely due to the strong dependence of dehydroascorbic acid ketal derivatives on trace metals for stability, since mutation of the copper binding ligands leads to lowered levels of copper in the sample. Consistent with this conclusion, close inspection of the spmoB_H137,139A (Cu_B ligating His residues mutated) optical spectrum reveals the presence of a small amount of 345 nm absorbance despite mutation of two of the three Cu_B His ligands (*30*). Conversely, the spmoB_H48N_137,139A (bis-His and Cu_B residues mutated) optical spectrum shows no evidence of 345 nm absorbance. The only difference between spmoB_H137,139A and spmoB_H48N_137,139A is mutation of the nonconserved bis-His residue His48. This mutation decreases the total amount of Cu bound by the protein by approximately 0.5 Cu equivalents (*27*). The reason this was not noted previously was likely the low intensity of the 345 nm feature in the spmoB_H137,139A optical spectrum.

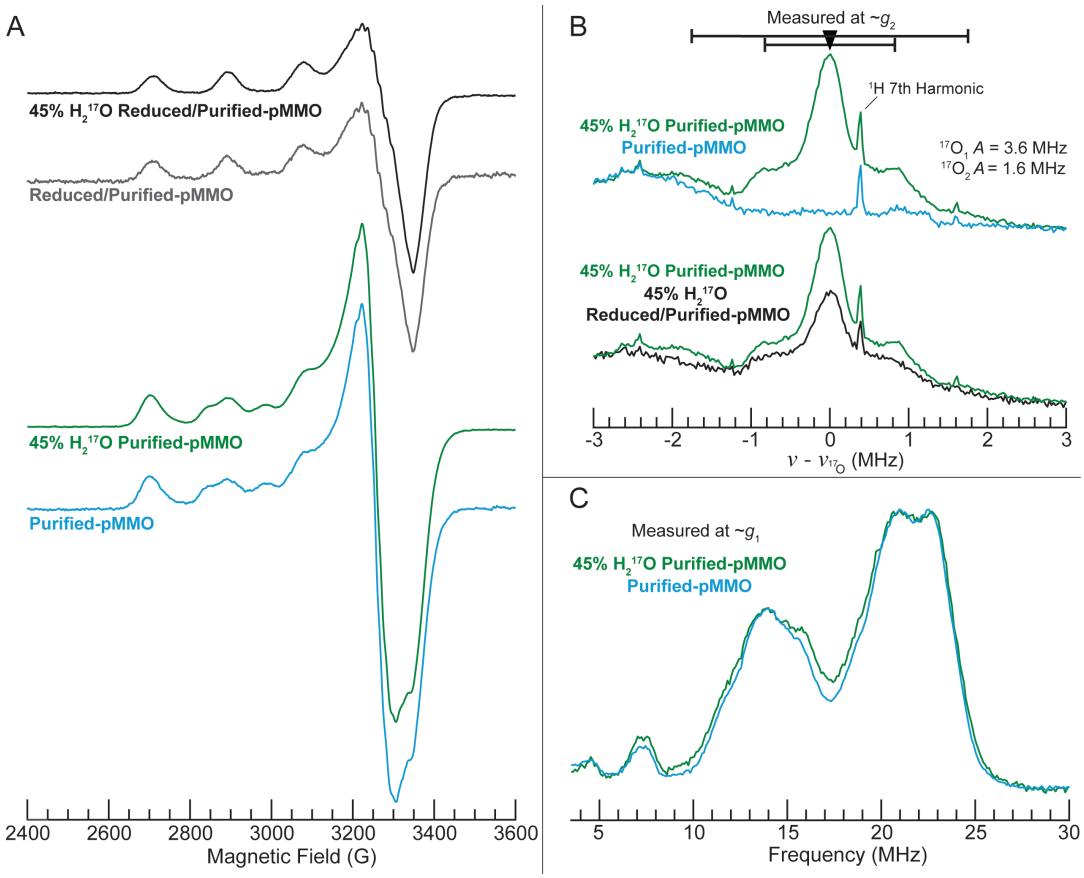

Fig. S6. EPR and ENDOR characterization of (all samples were natural abundance N and Cu) Purified- and Purified/Reduced-pMMO with $H_2{}^{17}O$. (**A**) X-band EPR measurements assessing Purified- and Purified/Reduced-pMMO, both in 45% $H_2{}^{17}O$ compared to natural abundance H_2O (~ 0% ^{17}O). If Cu_B(II) featured an equatorial H_xO ligand, both $H_2{}^{17}O$ Purified- and $H_2{}^{17}O$ Purified/Reduced-pMMO would exhibit broadening of the ^{14}N hyperfine lines relative to the natural abundance H_2O samples, due to the large hyperfine coupling to the ^{17}O (approximately equivalent to that of an equatorial N ligand) (*61*). However, neither sample exhibits such broadening. ***Conditions***: 9.36-9.37 GHz microwave frequency, 90 s scan rate, 320 ms time constant, 12.5 G modulation amplitude, temperature 20 K. Protein concentrations of natural abundance Purified- and Reduced/Purified-pMMO were 167 µM. (**B**) Mims ^{17}O-Larmor centered ENDOR testing for weakly-coupled ^{17}O on Cu_B and Cu_C. The ^{17}O hyperfine coupling A = 1.6 MHz observed in both $H_2{}^{17}O$ Purified/Reduced-pMMO and Purified-pMMO is of the magnitude expected for an axial H_xO ligand (*62*). Thus, there exists an axially coordinated H_2O on Cu_B. The larger coupling ^{17}O A = 3.6 is attributed to a H_xO coordinated to Cu_C. ***Conditions***: 34.6-34.7 GHz microwave frequency, 20 ms repetition time ($H_2{}^{17}O$ Purified-pMMO and natural abundance Purified-pMMO), 100 ms repetition time ($H_2{}^{17}O$ Purified/Reduced-pMMO), π = 100 ns, T_{RF} = 60 µs, τ = 1400 ns and RF tail = 10 µs. (**C**) The equivalence of the Davies ENDOR responses between natural abundance and $H_2{}^{17}O$ Purified-pMMO samples in this region indicates that Cu_B does not feature an equatorial $H_x{}^{17}O$ ligand whose coupling would be ~30-33 MHz (^{17}O Larmor frequency $\nu_{^{17}O}$ = 6.4 MHz) as shown previously (*61*). ***Conditions:*** 34.5-34.7 GHz microwave frequency, 20 ms repetition time, π = 80 ns, T_{RF} = 15 µs, τ = 475 ns, RF tail = 5 µs.

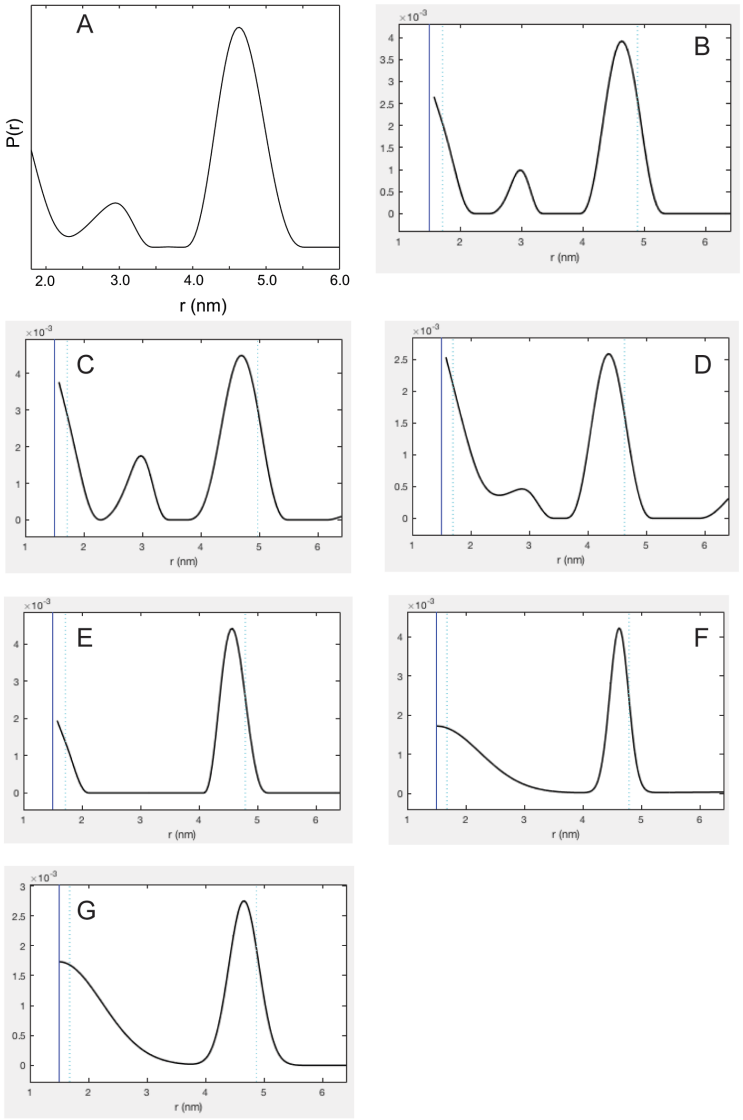

Fig. S7. Alternative analyses of DEER distance distributions showing that the feature at 4.5 nm is robust to analysis procedure, whereas the 2.8 nm feature is highly variable. The distribution shown in (**A**) is the same as that presented in Fig. 3. *Analysis procedures*: (**A**) manually optimized phase correction, zero time, using a 3rd order homogenous background function, followed by Tikhonov regularization. (**B**) Automatic phase correction, zero time, using a 2nd order homogenous background function, followed by Tikhonov regularization. (**C**) Automatic phase correction, zero time, using a 1st order polynomial background function, followed by Tikhonov regularization. (**D**) Automatic phase correction, zero time, using a 2nd order polynomial background function, followed by Tikhonov regularization. (**E**) Manually optimized phase correction, zero time, using a 2nd order homogenous background function, followed by Tikhonov regularization. (**F**) Automatic phase correction, zero time, using a 1st order polynomial background function, followed by 2 Gaussian fit function. (**G**) Automatic phase correction, zero time, using a 1st order polynomial background function, followed by 2 Gaussian homogeneous fit function.

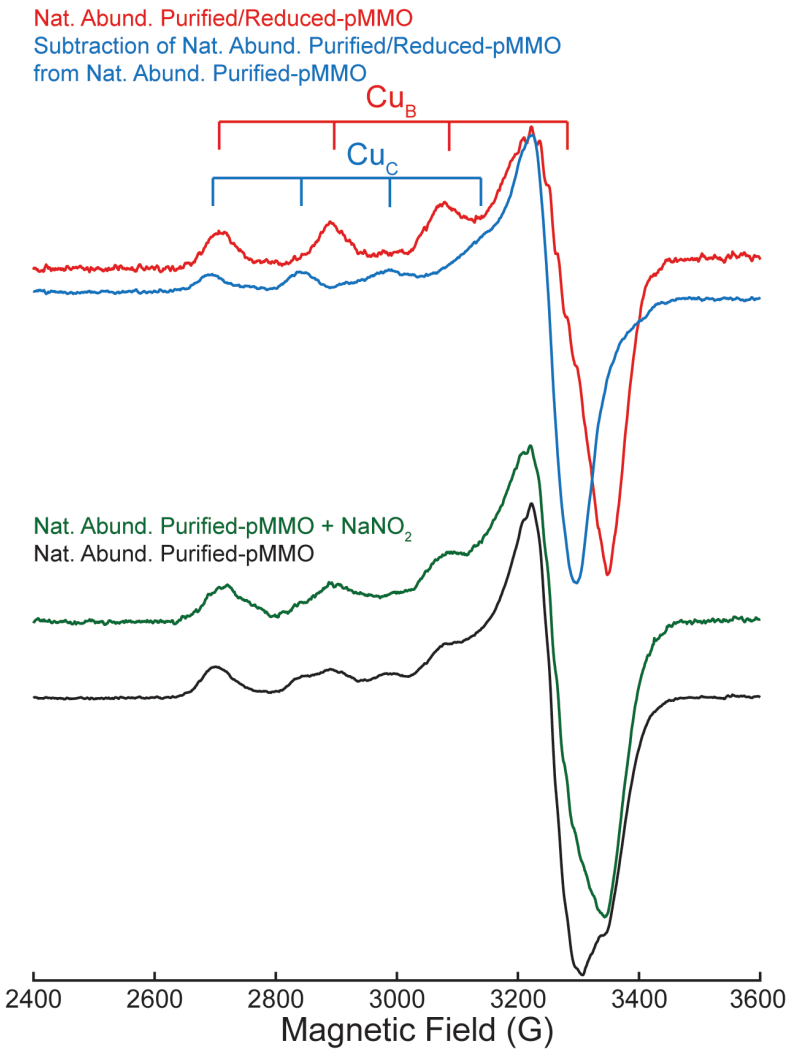

Fig. S8. Natural abundance Purified-pMMO before and after incubation with 2 M $NaNO_2$. Nitrite-induced changes to the Cu_C(II) EPR signal are most evident in the $g_\perp$ region (~3300 G), a collapse of the otherwise resolved features. ***Conditions:*** 9.365 GHz microwave frequency, 90 s scan rate, 320 ms time constant, 12.5 G modulation amplitude, temperature 20 K. Purified- and Purified/Reduced-pMMO protein concentrations were 167 μM, while the Purified-pMMO sample after nitrite incubation was 83 μM.

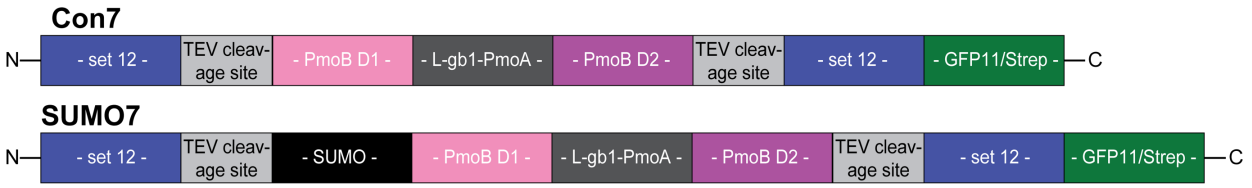

Fig. S9. Designed spmoB constructs used in ^{13}C-methane oxidation activity assays. The PmoB subdomain 1 (PmoB D1) is joined to PmoB subdomain 2 (PmoB D2) by L-gb1-PmoA rather than the flexible linker used to join the two subdomains in spmoB. GFP11 corresponds to the fragment of GFP utilized for the split GFP assay, and Strep refers to the Strep-tag.

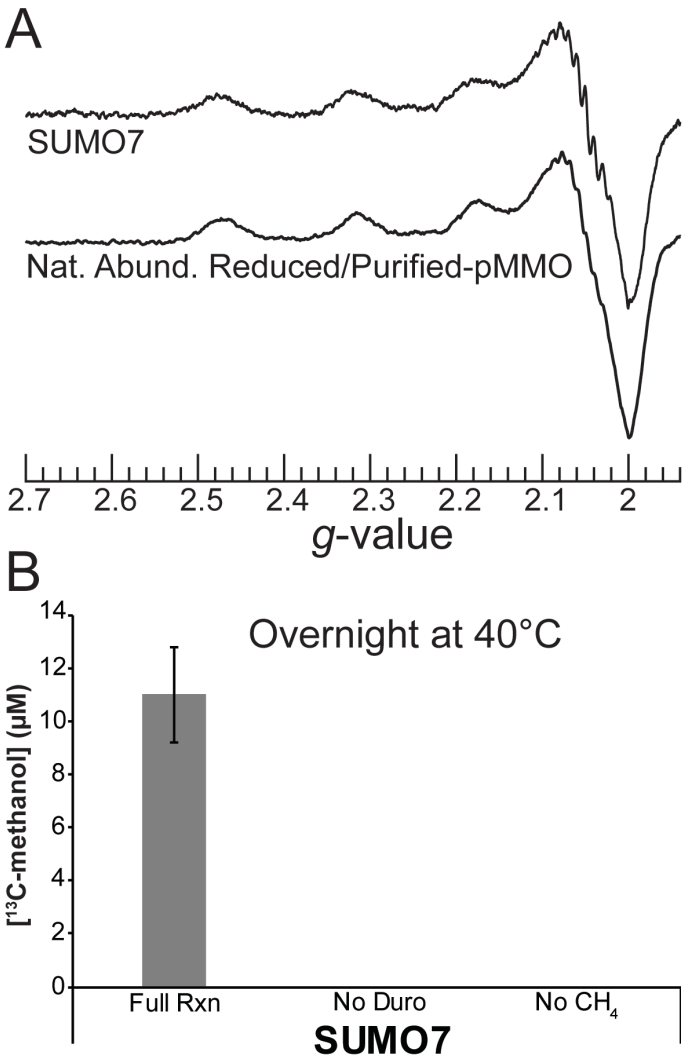

Fig. S10. Refolded SUMO7 and natural abundance Reduced/Purified-pMMO X-band EPR spectra, and SUMO7 ^{13}C-methane oxidation activity. (**A**) The inactive SUMO7 exhibits a Cu_B(II) EPR signal, similar to Reduced/Purified-pMMO although the Cu_B(II) site formed in SUMO7 cannot be identical to that of Reduced/Purified-pMMO since the N-terminal residue of SUMO7 is not His33 (and thus His33 cannot coordinate via both side chain and amine). ***Conditions:*** The SUMO7 and Reduced/Purified-pMMO concentrations are 250 and 167 μM, respectively. Spectra normalized to unity. SUMO7, 9.125 GHz microwave frequency, 1 min scan rate, 30 ms time constant, 4 G modulation amplitude, 77 K temperature; natural abundance Reduced/Purified-pMMO, 9.367 GHz microwave frequency, 90 s scan rate, 320 ms time constant, 12.5 G modulation amplitude, 20 K temperature. (**B**) ^{13}C-methane oxidation activity assay of the same batch of refolded SUMO7 as probed by EPR in (**A**). The SUMO7 protein concentration was 50 μM. SUMO7 does not exhibit methane oxidation activity above that observed for control reactions which do not feature Cu_B (e.g. NeMCO and Con7_3A in Fig. S11). Error bars indicate n = 3 replicates of reaction assay samples.

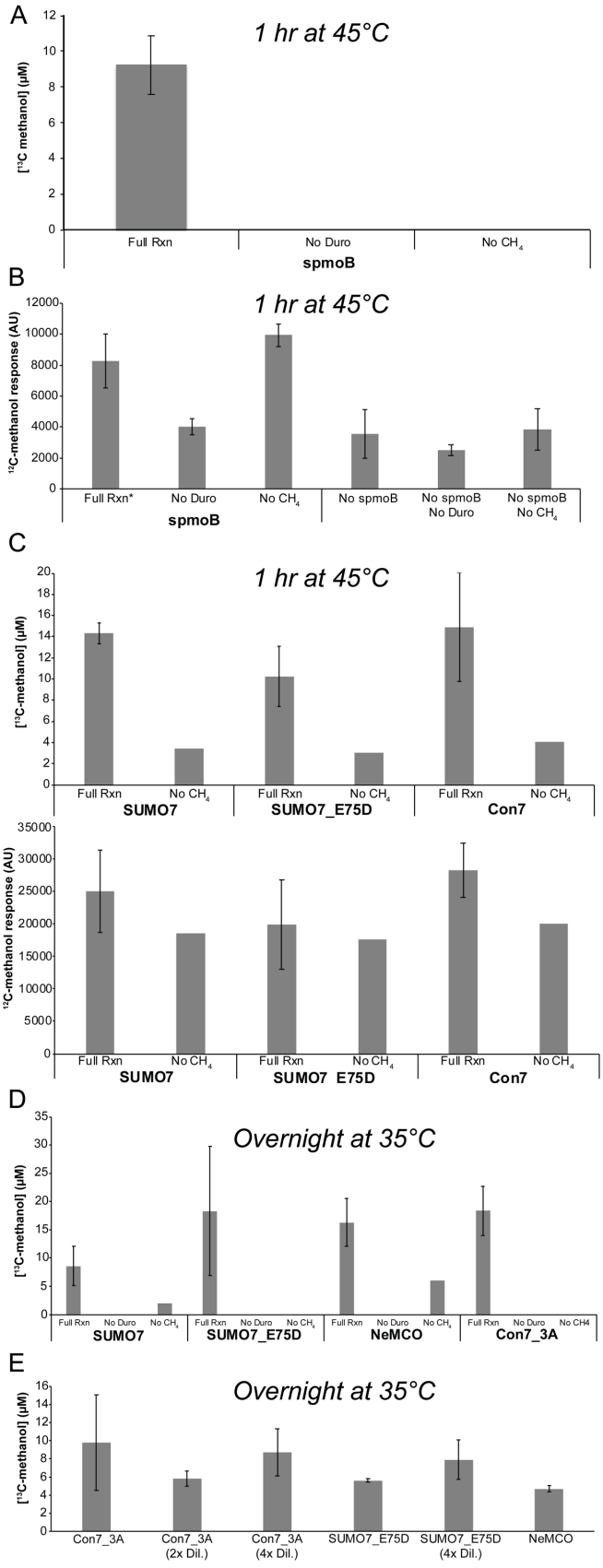
A
1 hr at 45°C
[13C methanol] (μM)
Full Rxn
No Duro
No CH4
spmoB
B
1 hr at 45°C
13C-methanol response (AU)
Full Rxn*
No Duro
No CH4
No spmoB
No spmoB No Duro
No spmoB No CH4
spmoB
C
1 hr at 45°C
[13C-methanol] (μM)
Full Rxn
No CH4
SUMO7
SUMO7_E75D
Con7
12C-methanol response (AU)
SUMO7
SUMO7 E75D
Con7
D
Overnight at 35°C
[13C-methanol] (μM)
No CH4
SUMO7
SUMO7_E75D
NeMCO
Con7_3A
E
Overnight at 35°C
[13C-methanol] (μM)
Con7_3A
Con7_3A (2x Dil.)
Con7_3A (4x Dil.)
SUMO7_E75D
SUMO7_E75D (4x Dil.)
NeMCO

* For 1 of the 4 "(+) spmoB, Full Rxn" replicates in (**B**), the entire MS-detected elution profile off the GC column was anomalous, so the replicate was omitted.

Fig. S11. Results of ^{13}C-methane oxidation activity assays performed on spmoB, its variants, as well as NeMCO. Representative assays in which appreciable ^{13}C-methanol was observed are shown. There were other assays run under the same conditions in which no samples showed any ^{13}C-methanol. Error bars indicate n ≥ 2 replicates of reaction assay samples. (**A**) Standard spmoB reaction time/temperature (*27*) generates ^{13}C-methanol from ^{13}C-methane, although the spmoB protein concentration (~30 μM) was lower than traditionally assayed for activity (~100 μM). (**B**) The ^{12}C-methanol absolute MS responses are consistently higher in samples containing both spmoB and duroquinol than in conditions with either individually or neither. While the ^{12}C-methanol levels are higher on average in the "(+) protein, No CH_4" than in the "(+) protein, Full Rxn" for this assay, this trend was often reversed, as shown in (**C**). In these such situations, where ^{12}C-methanol was produced over the course of the assay and the "(+) protein, Full Rxn" sample accumulated more ^{12}C-methanol than the "(+) protein, No CH_4" control, the spmoB construct would have appeared active using the GC-FID method of total methanol quantitation, as performed previously (*17, 27*). The differences in ^{12}C-methanol levels for samples containing both spmoB and duroquinol can be attributed to minor differences in the amount of duroquinol added since standard protocol calls for addition of a small scoop of this insoluble compound. Moreover, ^{12}C-methanol is a common contaminant in many buffer reagents. As ^{13}C represents ~1% of natural abundance carbon, we monitored ^{12}C-methanol levels to ensure that any ^{13}C-methanol observed after reaction was a product of methane oxidation, and not merely observation of the natural abundance ^{13}C-methanol from ^{12}C-methanol contamination. The spmoB protein concentration was 100 μM. (**C**) ***Top***: ^{13}C-methanol produced via spmoB construct reaction with ^{13}C-methane, with ***bottom***: ^{12}C-methanol responses. Con7, SUMO7, and SUMO7_E75D protein concentrations were 22 μM, 6 μM, and 17 μM, respectively. (**D**) ^{13}C-methane oxidation activity assays run overnight on several spmoB constructs as well as NeMCO. The activity detected for spmoB variant constructs is comparable to that observed for an unrelated enzyme (NeMCO) or a variant in which all three Cu_B His ligands are replaced with Ala (Con7_3A). SUMO7, SUMO7_E75D, NeMCO, and Con7_3A protein concentrations were 114 μM, 118 μM, 60 μM, and 131 μM, respectively. (**E**) ^{13}C-methane oxidation activity of diluted samples. There is no dependence on protein concentration. Initial Con7_3A, SUMO7_E75D, and NeMCO protein concentrations (prior to dilution) are same as in (**D**).

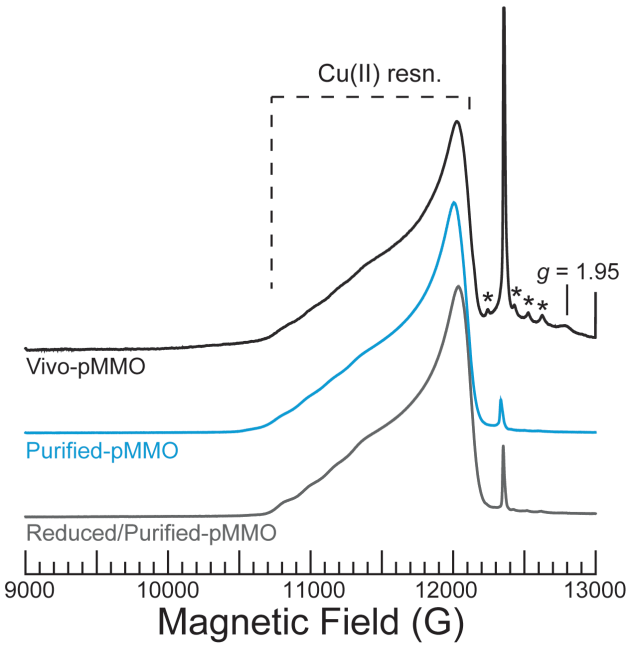

Fig. S12. Rapid-passage Q-band absorption-display CW EPR spectra of the 3 EPR samples shown in Fig. 1 and 2. The Cu(II) resonance is by far the dominant paramagnetic species. We note the extremely weak $g \sim 1.95$ feature in Vivo-pMMO, the intensity of which is exaggerated in the derivative-display of the X-band spectrum in Fig. 1 (~3470 G); this feature contributes negligible integrated intensity. Asterisks denote the hyperfine lines for the small amount of Mn^{2+} ($I = 5/2$). ***Conditions***: (Purified- and Reduced/Purified-pMMO) ~34.8 GHz microwave frequency, 2 min and 45 second scan rate, 64 ms time constant, 1 G modulation amplitude, temperature ~ 2 K. (Vivo-pMMO) is the same as the others except scan rate was twice as fast.

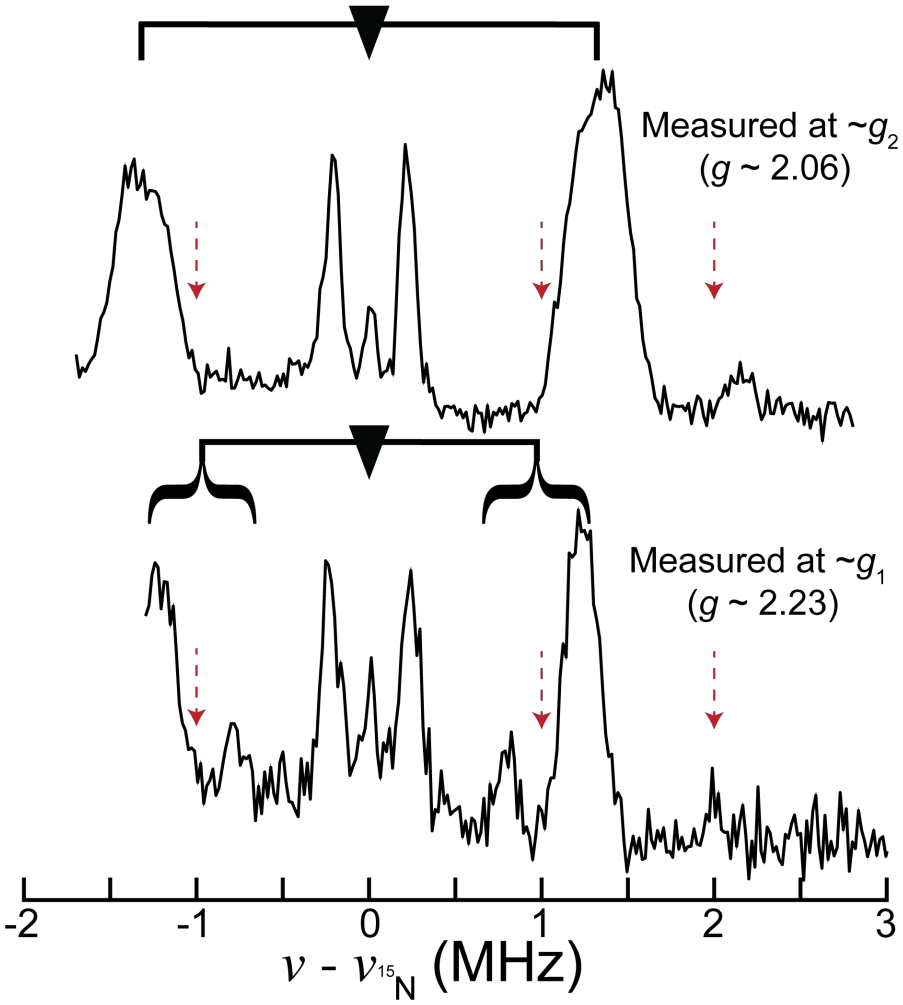

Fig. S13. Vivo-pMMO weakly-coupled ^{15}N Mims ENDOR showing both ν_+ and ν_- resonance, measured at g_1 and g_2. Triangle defines $\nu_{^{15}N}$ and goalpost splittings define ν_+ and ν_- partners; red arrows denote Mims "holes". For the Mims pulse sequence, the ENDOR response (R) is defined by the equation $R \sim 1 - \cos(2\pi A\tau)$. Consequently, for all integer values of $A\tau$ the ENDOR response/intensity is 0, leading to the so-called Mims "holes". For both ^{15}N-Larmor corrected spectra above, τ was chosen such that Mims holes appear every $|A|$ = Z(2 MHz), where Z is an integer. The g_1 ^{15}N ν_+ and ν_- responses both show such Mims holes (at $\nu_{^{15}N}$ ±1 MHz), confirming their assignment to weakly-coupled ^{15}N resonance. We note these must be Mims holes, as Fig. 2 indicates that for appropriate values of τ, ^{15}N resonance is non-zero at this frequency. The microwave amplifier employed for these measurements cannot measure frequencies low enough to observe the full ν_- peak at g_1. Collection conditions: 34.64 GHz microwave frequency, 50 ms repetition time, π = 100 ns, τ = 500 ns, T_{RF} = 60 µs, and RF tail = 10 µs.

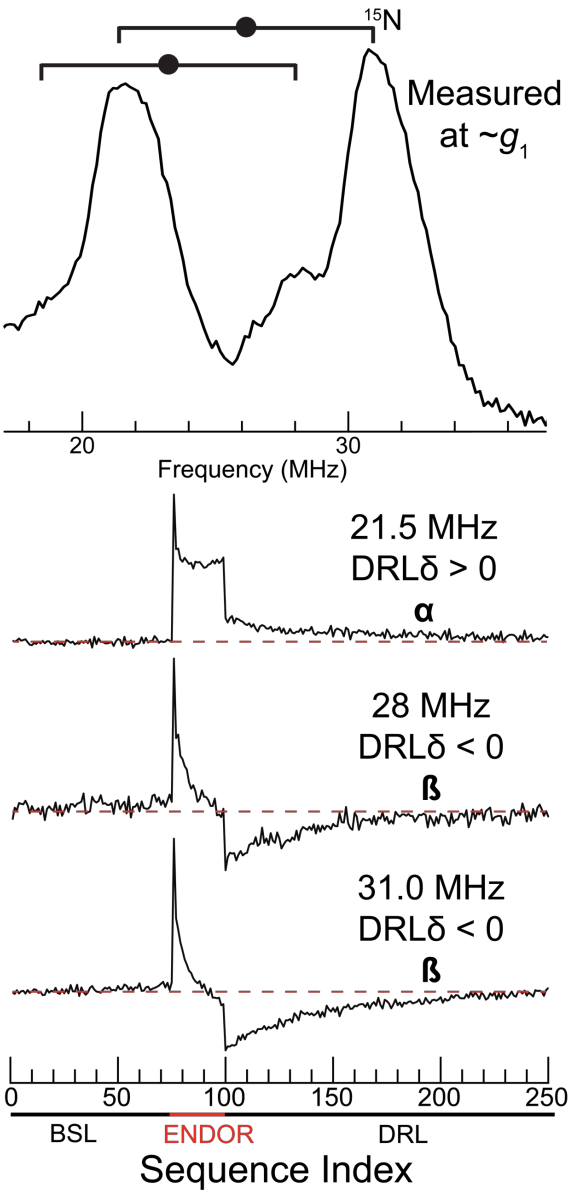

Fig. S14. PESTRE hyperfine sign assignments for strongly-coupled ^{15}N resonance in Vivo-pMMO. ***Top***: Davies ENDOR measurements defining the ^{15}N resonance at g_1. ***Bottom***: PESTRE responses measured at measured at g_1. The PESTRE experiment utilizes three discrete Davies ENDOR sequences. First, a baseline signal is established (BSL) during which time the microwave is applied with no RF, saturating the EPR transition. Next, a single frequency RF is applied to saturate the ENDOR transition (ENDOR). Finally, the RF is turned off (DRL) and the direction of echo relaxation relative to the BSL (DRLδ ≡ DRL - BSL) defines the manifold producing the observed resonance (labeled as α or β to indicate the higher or lower energy electron spin manifolds, respectively). For ν_+ DRLδ > 0, $A/g_n < 0$, while ν_+ DRLδ < 0 defines $A/g_n > 0$; likewise, for ν_- DRLδ < 0, $A/g_n < 0$, while ν_- DRLδ > 0 defines $A/g_n > 0$. Consequently, as expected, the PESTRE measurements are consistent with exclusively strongly-coupled ^{15}N $A/g_n > 0$, indicating a positive spin density $\rho > 0$ since $\rho \propto A/g_n$. Collection conditions: 34.5-34.6 GHz microwave frequency, 100 ms repetition time, π = 80 ns, τ = 600 ns, T_{RF} = 15 μs, and RF tail = 5 μs.

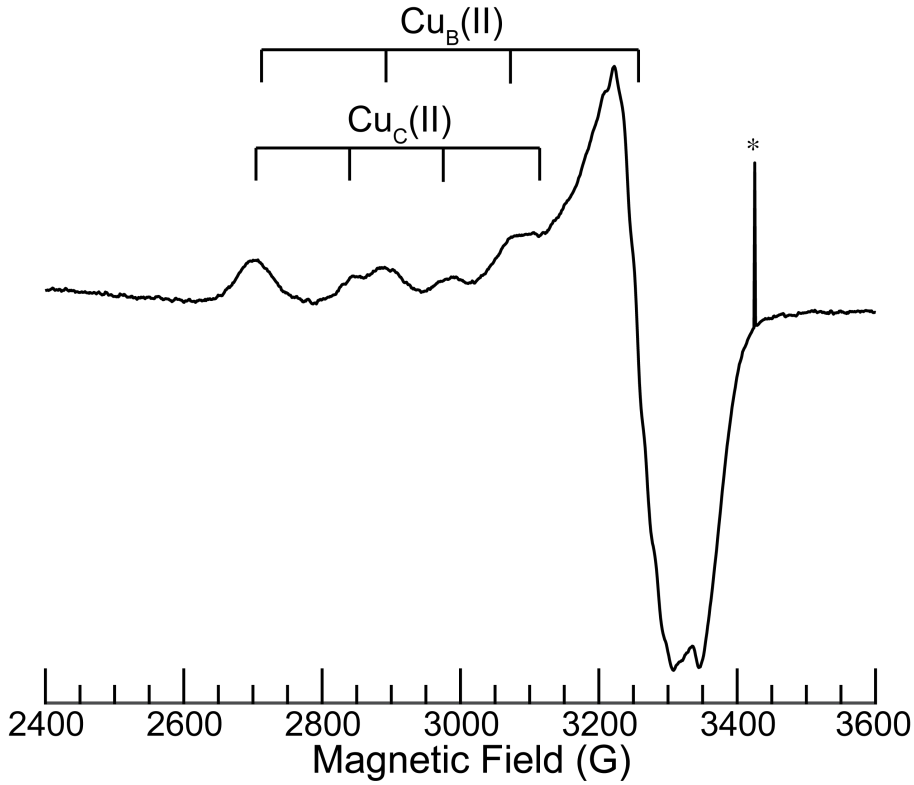

Fig. S15. X-band CW EPR of the Purified-pMMO sample used for DEER measurements (buffer conditions: 50 mM PIPES, 500 mM NaCl, 0.04% DDM, pH 7.2). Bracket width denotes A_1 Cu hyperfine splitting, and the center of the brackets indicate g_1 using the values from Table S1. Asterisk denotes an instrument artifact sometimes observed on the spectrometer. The altered buffer conditions do not alter the Cu_B(II) or Cu_C(II) signals from those observed under the standard Purified-pMMO buffer conditions (as in Fig. 1). Collection conditions: 9.366 GHz microwave frequency, 90 s scan rate, 320 ms time constant, 12.5 G modulation amplitude, 20 K temperature, 5 scans.

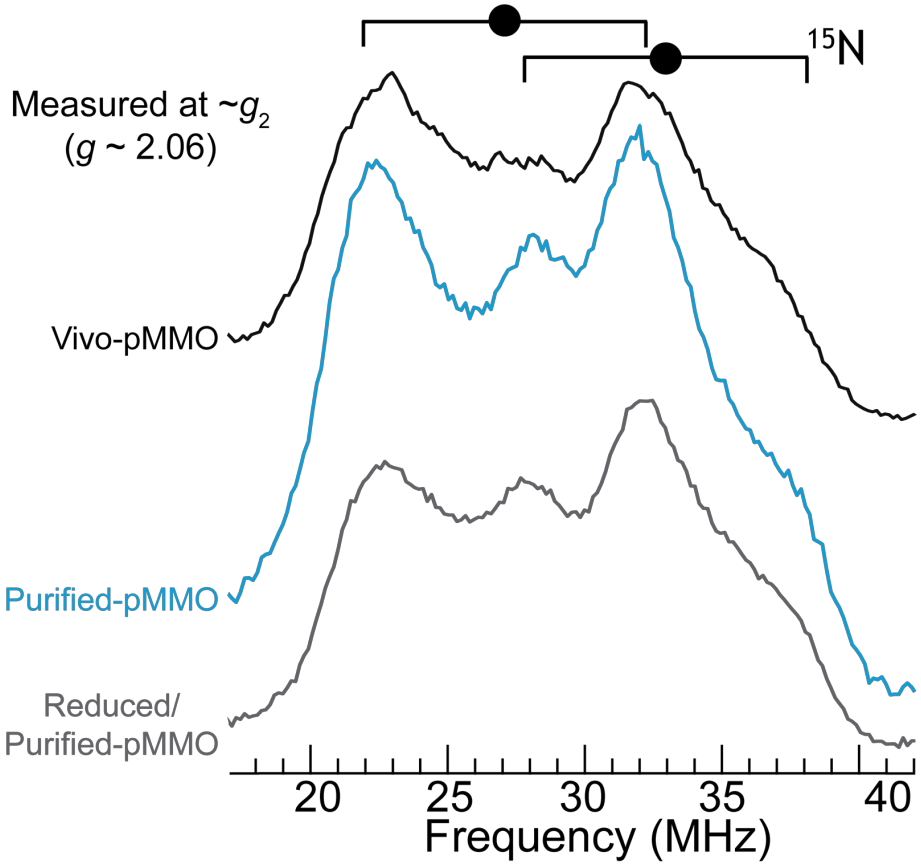

Fig. S16. ^{15}N Davies ENDOR measured at g_2 for Vivo-, Purified-, and Reduced/Purified-pMMO. Intensities normalized to match those of ^{15}N in Fig. S3A. Goalpost width indicates twice the ^{15}N Larmor frequency ($\nu_{^{15}N}$), filled circle defines half the hyperfine coupling magnitude ($|A/2|$). Collection conditions: 34.5-34.7 GHz microwave frequency, 50 ms repetition time, π = 80 ns, τ = 400 ns, T_{RF} = 15 µs, and RF tail = 5 µs.

References and Notes:

40. R. L. Lieberman *et al. Proc. Natl. Acad. Sci. U.S.A.* **100**, 3820-3825 (2003).
41. H. Yuan, M. L. P. Collins, W. E. Antholine. *Biophys. J.* **76**, 2223-2229 (1999).
42. C. D. Blanchette *et al. Nat. Commun.* **7**, 11900 (2016).
43. S. Cabantous, G. S. Waldo. *Nat. Methods* **3**, 845 (2006).
44. Y.-B. Zhang *et al. Protein Expr. Purif.* **36**, 207-216 (2004).
45. M. P. DeLisa, D. Tullman, G. Georgiou. *Proc. Natl. Acad. Sci. U.S.A.* **100**, 6115-6120 (2003).
46. A. C. Fisher, W. Kim, M. P. Delisa. *Protein Sci.* **15**, 449-458 (2006).
47. J. Li *et al. Biotechnol. J.* **11**, 212-218 (2016).
48. F. W. Studier. *Protein Expr. Purif.* **41**, 207-234 (2005).
49. J. A. Zahn, A. A. DiSpirito. *J. Bacteriol.* **178**, 1018-1029 (1996).
50. S. Stoll, A. Schweiger. *J. Magn. Reson.* **178**, 42-55 (2006).
51. C. E. Davoust, P. E. Doan, B. M. Hoffman. *J. Magn. Reson. Series A* **119**, 38-44 (1996).
52. B. Epel, I. Gromov, S. Stoll, A. Schweiger, D. Goldfarb. *Concepts Magn. Reson. Part B Magn. Reson. Eng. Engineering* **26**, 36-45 (2005).
53. P. E. Doan, B. M. Hoffman. *Chem. Phys. Lett.* **269**, 208-214 (1997).
54. P. E. Doan. *J. Magn. Reson.* **208**, 76-86 (2011).
55. N. C. Eickman, R. S. Himmelwright, E. I. Solomon. *Proc. Natl. Acad. Sci.* **76**, 2094-2098 (1979).
56. M. Pretzler, A. Rompel. *Inorg. Chim. Acta* **481**, 25-31 (2018).
57. A. S. Hakemian *et al. Biochemistry* **47**, 6793-6801 (2008).
58. R. J. Gurbiel *et al. J. Am. Chem. Soc.* **115**, 10888-10894 (1993).
59. N. Atherton, A. Horsewill. *Mol. Phys.* **37**, 1349-1361 (1979).
60. H. Goldenberg *et al. Anal. Chem.* **66**, 1086-1089 (1994).
61. D. Getz, B. L. Silver. *J. Chem. Phys.* **61**, 630-637 (1974).
62. D. Kim, N. H. Kim, S. H. Kim. *Angew. Chem. Int. Ed.* **52**, 1139-1142 (2013).